Materials Today Bio 32 (2025) 101699

Contents lists available at ScienceDirect

Materials Today Bio

journal homepage: www.journals.elsevier.com/materials-today-bio

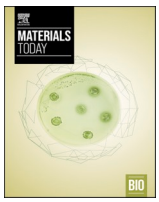

Magnetic scaffolds for the mechanotransduction stimulation in tendon tissue regeneration

Eleonora Bianchi [a], Manuel Bañobre-Lopez [b], Marco Ruggeri [a], Elena Del Favero [c], Barbara Vigani [a], Caterina Ricci [c], Cinzia Boselli [a], Antonia Icaro Cornaglia [d], Martin Albino [e,f], Claudio Sangregorio [e,f], Alessandro Lascialfari [g], Jessica Zanovello [h], Eugenio Jannelli [h,i], Francesco Claudio Pavesi [h], Silvia Rossi [a], Luca Casettari [j], Giuseppina Sandri [a,*]

[a] Department of Drug Sciences, University of Pavia, Viale Taramelli 12, 27100, Pavia, Italy
[b] International Iberian Nanotechnology Laboratory-INL, Braga, Portugal
[c] Department of Medical Biotechnology and Translational Medicine, University of Milan, LITA Viale Fratelli Cervi 93, 20090, Segrate, Italy
[d] Department of Public Health, Experimental and Forensic Medicine, University of Pavia, via Forlanini 2, 27100, Pavia, Italy
[e] CNR-ICCOM, Sesto Fiorentino, Italy
[f] Department of Chemistry "U. Schiff", University of Florence and INSTM, I-50019, Sesto Fiorentino, FI, Italy
[g] Department of Physics, University of Pavia and INFN section, Via Agostino Bassi 6, 27100, Pavia, Italy
[h] Orthopedics and Traumatology Clinic, IRCCS Policlinico San Matteo Foundation, 27100, Pavia, Italy
[i] Department of Clinical, Surgical, Diagnostic and Pediatric Sciences, University of Pavia, 27100, Pavia, Italy
[j] Università degli Studi di Urbino Carlo Bo, Urbino, Italy

ARTICLE INFO

Keywords:
Tendon disorders
Magnetite nanoparticles
Mechanotransduction
Polyhydroxybutyrate
Gelatin
Magnetic scaffolds
Centrifugal spinning

ABSTRACT

Nowadays, tendon injuries represent a global health issue that annually affects millions of individuals. An innovative approach for their treatment is represented by the development of tissue engineered scaffolds able to support the host cells adhesion, differentiation, and proliferation. However, the scaffold alone could be insufficient to guarantee an improvement of healing control. Magnetite nanoparticles (Fe_3O_4 NPs) are gaining interest due to their unique properties. In particular, when combined with bio-mimetic scaffolds, they should lead to the cells mechano-stimulation, improving the tenogenic differentiation and allowing a deeper tissue reparation.

The aim of this work is the study and the development of scaffolds based on polyhydroxybutyrate and gelatin and doped with Fe_3O_4 NPs. The scaffolds are characterized by an aligned fibrous shape able to mimic the tendon fascicles. Moreover, they possess a superparamagnetic behavior and a slow degradation rate that should guarantee structural support during the tissue regeneration. The magnetic scaffolds promote cell proliferation and alignment onto the matrix, in particular when combined with the application of an external magnetic field. Also, the cells are able to differentiate and produce collagen I extracellular matrix. Finally, the magnetic scaffold *in vivo* promotes complete tissue healing after 1 week of treatment when combined with the external magnetic stimulation.

1. Introduction

Nowadays, tendon injuries represent a global health issue that annually affects millions of individuals. As a result, tendon injuries place a significant clinical load on health systems due to the high costs of procedures, rehabilitation, and infiltrations [1,2]. In clinic, the reconstruction of tendon defects secondary to trauma or intrinsic tissue degeneration is still difficult for surgeons, especially due to the poor healing ability of the tissue, which often leads to re-rupture or debilitating impairments [3,4].

In recent years, the great scientific advances occurred in fields such as materials engineering and bio- and physico-chemistry have led to the application of tissue engineering approaches for the treatment of orthopaedic injuries, aiming at the regeneration of the damaged tissues [2,

* Corresponding author.
E-mail address: g.sandri@unipv.it (G. Sandri).

https://doi.org/10.1016/j.mtbio.2025.101699
Received 17 January 2025; Received in revised form 7 March 2025; Accepted 22 March 2025
Available online 26 March 2025

4]. In fact, the development of tissue engineered bio-mimetic scaffolds able to support the host cells adhesion, differentiation, and proliferation results as a promising approach for the treatment of tendon injuries. However, the scaffold alone is insufficient to guarantee an improvement of healing control [5,6]. In fact, the cells should migrate on their own onto the scaffold after the implant in order to start its replacement with the native tissue. On the other hand, the application of an external magnetic field could be a great tool to guarantee a complete healing control by guiding and stimulating the cells.

Recently, magnetic nanoparticles (MNPs), including magnetite (Fe_3O_4) and maghemite (Fe_2O_3), have gained great interest due to their biocompatibility and unique magnetic properties [7,8]. In fact, these NPs are approved by the Food and Drug Administration for a wide variety of applications, including local thermal therapy for tumors, contrast agents, and iron replacement therapies [9]. Recently, their potential in tissue repair in combination with scaffolds has also been investigated. Preliminary investigations seem to suggest that the inclusion of magnetic NPs into the scaffolds could results in the control of cell signalling both *in vitro* and *in vivo* [8,10]. The supposed mechanism is the mechano-stimulation. In fact, the nano-movements induced by the application of an external magnetic field on the NPs seems able to cause forces in the range of pN, and cells act in response to those mechanical stimuli allowing a deeper tissue reparation and stimulating the tenogenic differentiation of stem cells and cell alignment [10]. Furthermore, their superparamagnetic behavior is of particular interest as the NPs lose magnetism after removing the field, allowing a precise remote control over their functions.

In literature, the potential of MNPs, and in particular of magnetic cell sheets, has been revealed as they demonstrated to enhance angiogenesis [11], and cardiac [12], bone [13], and skeletal muscle regeneration [14]. More recently, other studies also reported the tenogenic potential of MNPs combined with an external magnetic field, as they improved the expression of tendon markers and the deposition of tendon-like matrix [15]. Tomás et al. combined a 300 mT dynamic magnetic field with scaffolds enriched with MNPs, leading to an improvement in the fibers alignment and to a mechanical stimulation of mesenchymal stem cells tenogenic differentiation [16]. In recent literature, static magnetic fields from 15 mT to 50 mT were also found to mechanically stimulate cells, leading to an increase of collagen I secretion and integrins expression, and, consequently, to an improve in osteogenesis [8,17]. However, the effect of magnetic fields of different extent combined with magnetic scaffolds on cells alignment and proliferation has not been fully investigated to date. In particular, the effect of static magnetic fields in mechanotransduction has not been widely investigated in tendon regeneration.

On the basis of these premises, the aim of this work was the design and the development of fibrous scaffolds based on polyhydroxybutyrate (PHB) and Fe_3O_4 MNPs. In particular, the present research aims at the improvement of the healing control thanks to the addition of MNPs, which provide a mechanical stimulation to which the tendon cells respond improving their alignment and ECM secretion.

PHB is the most widely studied member of the polyhydroxyalkanoates family, produced by numerous microorganisms, including Gram–positive and Gram–negative bacteria, under conditions with limited nutrients (such as potassium, magnesium, ammonium and phosphate), and excessive availability of carbon. These unbalanced nutrients result in an excessive intracellular storage, which are collected as PHB granules [18,19]. In the last decades, PHB has attracted great attention in a wide variety of medical applications, such as surgical sutures, orthopaedic uses, and cardiac substitutes, together with tissue engineering [20]. In particular, PHB is of particular interest since it shows excellent barrier capacity, and tunable mechanical properties based on its molecular weight and level of crystallinity [18,21]. Moreover, it also demonstrated good cell adhesion and proliferation with a wide variety of human cells, such as fibroblasts, hepatocytes, and endothelium cells. This is probably due to the fact that it has been found in cellular membranes of animals, and also in human blood [22,23]. Interestingly, PHB degradation product, the 3 hydrobutyric acid, has been demonstrated to be a natural human metabolite found in brain, lungs, liver, heart, kidneys, and muscular tissue [23]. Moreover, the appropriate degradation period of scaffolds for tendon tissue engineering is crucial for ensuring that the scaffold supports tissue regeneration while gradually being replaced by new tissue. Research indicates that the ideal degradation time should align with the rate of new tissue formation, typically ranging from several weeks to a few months. In particular, scaffolds should provide structural support within 3 months from the surgery [24]. At this purpose, PHB results an interesting polymer for tendon reconstruction also due to its long degradation rate *in vivo* (3–6 months).

In this work, the PHB scaffold was also enriched with gelatin (Gel), as it is a derivative of collagen able to sustain cell adhesion and proliferation typical of collagen without immunogenicity [25,26]. In particular, the addition of Gel is intended to stimulate the cell adhesion onto the scaffolds and consequently their proliferation, overcoming the PHB hydrophobicity.

The developed scaffold should emulate the structural and biomechanical functions of the extracellular matrix (ECM) of the native tendons. Moreover, it should respond to the stimulation of an external magnetic field improving the host cell adhesion and proliferation allowing a deeper tissue replacement.

2. Experimental section

2.1. Materials

Polymers: Poly 3-hydroxybutyrate (Biomer® P209, Biopolyesters), and Gel (P5 150 medium alkaline Bloom gelatin, 160 gelling strength, Rousselot Gelatin S.L.U., Paratge Pont de Torrent, Spain) were employed. Fe_3O_4 NPs were synthesized by thermal decomposition of iron acetylacetonate ($Fe(acac)_3$), in high-boiling solvent (benzyl ether) in the presence of surfactants (oleic acid, OA; oleylamine, OAM), which has emerged as extremely effective in the formation of MNPs with excellent results in terms of size distribution, morphology and crystallinity. The synthesis and characterization of Fe_3O_4 NPs coated with oleic acid (Fe_3O_4@OA) are reported in the Supporting Information (Figs. S4 and S5).

2.2. Preparation of the polymeric blends

Table 1 reports the composition of the polymeric blends used to obtain the corresponding scaffolds. PHB was dissolved in acetic acid (Carlo Erba Reagents, Val-de-Reuil Cedex, France) under magnetic stirring for 20 min at 90 °C. At first, different percentages of PHB were used to evaluate the influence of the polymer concentration on the spinning process and fibers morphology. The concentration that allowed the fine formation of homogeneous fibers was selected to be enriched with Fe_3O_4@OA and Gel. The safe quantity of MNPs to be loaded was preliminarily determined by a cytotoxicity test (Supporting Information, Section 2.2).

Table 1
Quali-quantitative composition of the polymeric blends. All blends were prepared in acetic acid

Blend	PHB (% w/w)	Gel (% w/w)	Fe_3O_4@OA (% w/w)
P8	8		
P20	20		
P30	30		
P20-Fe_3O_4	20		0.2
P20-Fe_3O_4-Gel	20	4	0.2

2.3. Scaffolds preparation

The scaffolds were manufactured using a customized centrifugal spinning equipment (Supporting Information, Fig. S1), equipped with an AC motor (230 V, 50 Hz and 1030 W), a rotator system consisting of an aluminium spinneret coupled with brass needles (Ø = 1 mm), a speed controller, a temperature controller coupled with a platinum sensor thermometer (PT-100) and a digital thermometer (from 20 to 300 °C). Finally, a static collector based on vertical steel bars was installed on the rotor system. The polymeric blends were spun at 125 °C in order to allow the complete solvent evaporation. The obtained scaffolds were insoluble in water.

In order to improve the scaffolds mechanical properties, the cord scaffolds were combined and manually braided to create a more complex-structured braid scaffold.

2.4. Scaffolds chemico-physical characterization

The scaffolds morphology was assessed by means of scanning electron microscope (SEM) analysis (Tescan, Mira3XMU, Brno, Czech Republich). The samples were sputtered with graphite. The fibers diameters were assessed by image analysis software (ImageJ, ICY, Institut Pasteur, Paris, France). At this purpose, to ensure that the measured fibers were randomly chosen and representative of the whole scaffold, 3 different images were used, performing 30 analyses each, with a final total of 90 analyses. Moreover, the inclusion of the MNPs into the fibrous structure was evaluated by means of SEM-EDX, recording an EDX spectrum.

The wettability of the scaffolds was assessed with a contact angle meter (DMe-211 Plus; FAMAS software, Kyowa, Osaka, Japan). The droplet shape (0.4 μL of PBS) was captured through the CCD camera at 1s and 3s after the droplet touched the scaffold surface.

2.5. Magnetic characterization

Hysteresis loops of the scaffolds were recorded in a superconducting quantum interference device magnetometer (SQUID-VSM, Quantum Design), with magnetic field ranging from −20 to + 20 kOe at 5 and 300 K (room temperature). Zero-field-cooled (ZFC) and field-cooled (FC) magnetization curves were also recorded with the same magnetometer over the temperature range of 5–300 K and under an applied magnetic field of 100 Oe. Around 10 mg of fibers were placed in gelatine capsules, introduced in standard straw sample holders and attached to the measuring rod. The magnetization units were expressed as emu per gram of analysed sample.

The effective % of embedded Fe_3O_4@OA NPs was calculated by means of ZFC-FC curves using the following formula:

$$\%\ Fe_3O_4@\text{OA}\ incorporated = \frac{Moment\ sample}{Moment\ Fe_3O_4\ nanoparticles} \times 100$$

2.6. Structural characterization

Differential scanning calorimetry (DSC) and thermogravimetric analysis (TGA) were performed by means of a TGA/DSC1 equipment (TGA/DSC1/1100 SF, Mettler-Toledo GMBH, Spain) equipped with a microbalance (precision 0.1 μg) and with a horizontal oven, in 25–900 °C temperature range and 10 °C/min heating rate, and in argon. A final plateau in atmospheric air at 900 °C for 30 min was performed in order to burn the whole organic content. Approximately 5 mg of each sample were weighted in aluminum sample pans.

Fourier-transform infrared spectroscopy (FT-IR) analysis was carried out using a Vertex 80v vacuum Fourier Transform Infrared apparatus (Bruker, Billerica, USA). The spectra were recorded from 400 to 4000 cm^{-1} with a resolution of 2 cm^{-1}.

The scaffolds' structure at the nanoscale was investigated by small angle x-ray scattering (SAXS). Measurements were performed at the ID02 high-brilliance beamline (ESRF, Grenoble, France) at room temperature [27]. Small pieces were cut from each scaffold (0.1 × 0.5 cm) along the alignment axis of the fibres, inserted in capillaries (ENKI, Concesio, Italy) and hydrated in water for 2 h before measurements.

The scattered radiation was acquired at two sample-to-detector distances. Appropriate angular regrouping was performed to obtain the scattered intensity profile as a function of the momentum transfer q in the q region $0.006 < q < 3\ nm^{-1}$.

2.7. Mechanical properties evaluation

The mechanical properties of the scaffolds were measured using a dynamometer (TA-XT plus, Stable Microsystems, Italy) equipped with a 5.0 kg load cell. Before testing, the scaffolds were cut 20 × 5 mm and the strips were clamped between two tensile grips (A/TG probe) setting an initial distance between the grips of 60.0 mm. Then, the upper grip was moved forward at a constant speed of 5.0 mm/s up to break. Mechanical properties were evaluated in dry and hydrated state, and force at break vs. distance was recorded.

The evolution of the structure at nanoscale under mechanical stress was investigated by SAXS measurements. Identical pieces of scaffolds (25 mm × 5 mm) were hydrated and mounted in a tensile stage (Linkam Tensile Cell TST350) with 15 mm gap at rest. The device was humidity controlled, to avoid dehydration of the polymer matrixes. Measurements of the scattered intensity were performed at increasing strain, with elongation steps of 0.5 mm, up to the breaking point. During the scattering measurements, the force to maintain each the set deformation was measured as a function of time to observe the stress relaxation process.

2.8. Scaffolds in vitro degradation

To assess *in vitro* degradation, each scaffold was weighed (around 10 mg) and placed in 2 mL of PBS (phosphate saline buffer pH 7.4, Sigma-Aldrich, Milan, Italy) at 37 °C. Samples were removed after 2, 4, 8 and 12 weeks from the solution, washed twice in distilled water, dried in an oven at 60 °C for 3h, assuring their complete drying, and reweighed. The weight loss (%) was calculated as the ratio between the weight after degradation and the initial weight [28]. At every time interval (2, 4, 8, and 12 weeks), the fibrous scaffolds morphology was evaluated using SEM, as previously described (paragraph 2.4), in order to evaluate the morphological changes during the degradation process.

2.8.1. Fe_3O_4@OA NPs release

For the evaluation of the iron release from the scaffolds, the supernatants collected from the *in vitro* degradation test after 2, 4, 8, and 12 weeks (as described in Section 2.8) were filtered with a 0.22 μm filter, and then an elemental analysis was performed in triplicate by a Varian 720-ES inductively coupled plasma - atomic emission spectrometer (ICP-AES). For the analysis, 1 mL of sample was digested in concentrated HNO_3 and in presence of H_2O_2 and analysed using germanium (Ge) as internal standard.

2.9. In vitro evaluation

Proliferation and cell viability were carried out using normal human dermal fibroblasts (NHDF from juvenile foreskin, PromoCell, WVR, Italy; 1st–5th passages), and human adipose stem cells (hASC, ZenBio, Durham, NC, USA; 1st–3rd passages).

hASC were chosen after an extensive investigation since they are widely utilized to evaluate scaffolds for tendon tissue engineering *in vitro*. Various research studies indicate that hASC can differentiate into tendon-like cells and produce extracellular matrix components when cultured in appropriate scaffold environments. In the work of Hordé et al. hASCs showed the ability to differentiate towards a tendon phenotype, producing ECM proteins and exhibiting visco-elastic

properties in a 3D culture system, indicating successful maturation of the tendon-like tissues [29]. Moreover, gene expression analysis revealed the upregulation of tendon-specific markers (such as Scleraxis, Tenomodulin, and collagen type I) during culture [30,31]. Various scaffold designs were also tested to assess tenogenic differentiation on hASC, indicating that they can be effectively used in tendon tissue engineering and regerative therapies [32].

NHDF were cultured using DMEM growth medium (Sigma-Aldrich, Italy) supplemented with 10 % v/v fetal bovine serum (FBS, Euroclone, Milan, Italy) and with 200 IU/mL penicillin/0.2 mg/mL streptomycin (Sigma-Aldrich, Milan, Italy). hASC were cultured in basal-α-MEM medium based on minimum essential medium (α-MEM, ZenBio, Durham, NS, USA), supplemented with 10 % v/v FBS, 0.22 % w/v bicarbonate, and 200 IU/mL penicillin/0.2 mg/mL streptomycin. Both cell types were grown into an incubator (CO_2 Incubator, PBI International, Milano, Italy) at 37 °C in a 5 % CO_2 atmosphere with 95 % relative humidity (RH).

2.9.1. Cell proliferation assay

Each scaffold (5 mm diameters, 0.2 mm thickness) was sterilized by UV radiation for 30 min and placed in a 96-well plate to perfectly cover the bottom. NHDF or hASC were seeded onto the scaffolds at a density of 2×10^4 cells/well density and re-incubated. After 3, 7, 14, and 21 days of contact with the scaffolds, the medium was removed, and 1 % (v/v) Aqua Bluer solution (MoBiTec Molecular Biotechnology, Goettingen, Germany) was diluted with the cell medium and added into the wells (100 μL). After 4h of incubation in dark at 37 °C, the Aqua Bluer solution was collected from the wells and transferred in a new plate. Each well was then refilled with the culture medium and left in culture again. The fluorescence intensity (FI) was recorded using a microplate reader (Synergy H1 Microtiter Plate Reader, Biotek, Santa Clara, USA) with λex = 540 nm and λem = 590 nm. The fluorescence intensity (FI) was directly related to cell viability.

The same assay was used to evaluate cell proliferation with the application of an external magnetic field.

Strong static magnetic fields were reported to have the potency of regulating the orientation of cells *in vitro* and *in vivo*, and also of enhancing their proliferation, both fundamental aspects of the tendon regeneration [8,33].

In order to evaluate the effect of magnetic fields of different extent onto the cells growth, 16 rod magnets (N40 magnetization, 10 mm height, Ø 6 mm, S-06-10-N; Supermagnet, Gottmadingen, Germany) and a 96-well plastic culture plate were used to create the lower static magnetic fields exposure system. Similarly, cube magnets (N48 magnetization, 12 mm height, W-12-N; Supermagnet, Gottmadingen, Germany) and a customized plastic plate (obtained by means of a 3D printer) were used to create the higher static magnetic fields (Supporting Information, Fig. S2). Desired field intensities were established by controlling the magnets position, using a Gaussmeter (475 DSP Gaussmeter, Lake Shore cryotronics, Westerville, USA) to measure the intensities in each well. The plates with magnets were then put under the plates where the cells were seeded onto the scaffolds. In the present study, three different intensities were selected for the investigation: 47 mT ± 3, 155 mT ± 5, and 285 mT ± 5, in order to observe the cells' reaction to different magnetic fields. The experiment was then conducted on both NHDF and hASC as described at the beginning of this section.

2.9.2. Cell morphology

The cell morphology after 21 days of contact with the scaffolds was investigated using Confocal Laser Scanning Microscope (CLSM, Zeiss LSM 780 Confocal Microscope, Oberkochen, Germany) after nuclei and cytoskeleton staining. Cells grown onto the scaffolds were fixed using a 4 % (v/v) formaldehyde solution in PBS for 2h at room temperature. The substrates were then washed three times with PBS. Cellular cytoskeleton was stained with Phalloidin-TRITC (red, Sigma-Aldrich, Burlington, Massachusetts, USA; 50 μL at 50 μg/mL in PBS in each well, contact time 40 min), and the cell nuclei were then stained with DAPI (blue, ProLong™ Gold Antifade Mountant with DNA Stain DAPI, ThermoFisher Scientific, Waltham, Massachusetts, USA; one drop in each well). To evaluate the hASC tenogenic differentiation, ECM was stained using anti-collagen I rabbit polyclonal antibody (Thermofisher, Monza, Italy; 100 μL/sample at 10 μg/mL in PBS) to immuno-label collagen I produced from hASC differentiated in TEN-1 (24 h contact time at 4 °C). The primary antibody was stained with ATTO 488 goat anti rabbit IgG (Sigma Aldrich, Milano, Italy), as secondary antibody (green) as described in a previous work [6]. Scaffolds were placed onto microscope slides and imaged with λex = 540 nm and λem = 570 nm for phalloidin-TRITC, λex = 360 nm and λem = 460 nm for DAPI, and λex = 501 nm and λem = 523 nm for ATTO 488 goat anti rabbit IgG. The acquired images were processed with a software (Fiji ImageJ).

The cell morphology after 21 days of contact with the application of the 155 mT magnetic field was also evaluated by SEM analysis (Phenom Pure Pro, ThermoScientific, Waltham, Massachusetts, USA). The scaffolds were fixed using a 4 % (v/v) formaldehyde solution in PBS for 2h at room temperature. Once dried, the scaffolds were mounted on SEM supports and sputtered with 5 nm of gold (LUXOR Au, Luxor-Tec Gmbh, Switzerland).

2.9.3. Pro-inflammatory immune response

An ELISA kit (Thermo Fisher, Italy) was used to evaluate the proinflammatory immune response by the quantification of the TNF-α (proinflammatory cytokine) secreted by hASC after 3, 7, 14, and 21 days of contact with the scaffolds. The method was linear (concentration range: 7.8–500 pg/mL; $R^2 > 0.995$). Lipopolysaccharide (LPS, 10 μg/mL for 24 h) was used as positive control [34].

2.9.4. Hemolysis test

The hemocompatibility of P20-Fe_3O_4-Gel was evaluated by hemolysis test *in vitro* [35]. Fresh blood was taken from mice, and a stock solution was prepared by diluting it with 0.9 % saline solution in a 4:5 vol ratio. 10 mg of scaffolds were then weighted and put in contact with 0.2 mL of the diluted blood. Sterile water was used as positive control, while 0.9 % saline solution was used as a negative control. The samples were put in an incubator at 37 °C for 1 h, then they were centrifuged at 3000 rpm for 5 min. Afterwards, the supernatants were collected, and their absorbance were recorded using a microplate reader (Synergy H1 Microtiter Plate Reader, Biotek, Santa Clara, USA) at 545 nm.

Hemolytic rate (HR %) was determined as follows:

$$HR(\%) = \frac{(OD_{TEST} - OD_{NEG})}{(OD_{POS} - OD_{NEG})} \times 100$$

where OD_{TEST} is the sample's absorbance, OD_{NEG} is the negative control's absorbance, and OD_{POS} is the positive control's absorbance.

2.10. In vivo evaluation

All animal experiments were carried out in full compliance with the standard international ethical guidelines (European Communities Council Directive 2010/63/EU). The study protocol was approved by the Local Institutional Ethics Committee of the University of Pavia for the use of animals and by ISS (Istituto Superiore di Sanità). 12 male Wistar rats (Envigo RMS S.r.l.) with weights ranging from 200 g to 250 g were anesthetized with equitensine at 3 mL/kg. All animals were monitored for the following 3 days by animal care.

2.10.1. Evaluation of systems efficacy

A transversal cut was surgically made on the mice's left Achilles tendon, in order to cause an acute partial injury of the tissue (Supporting Information: Fig. S3). The P20-Fe_3O_4-Gel scaffold was implanted in order to fill the cut. The same cut was made on the right Achilles tendon,

which was treated with traditional suture.

2 different groups composed of 6 mice each were involved: the first group of 6 mice was treated with traditional suture (right Achilles tendon) and with the scaffold (left Achilles tendon) without the application of an external magnetic field; the second group of 6 mice was treated with traditional suture (right Achilles tendon) and with the scaffold (left Achilles tendon) with the application of an external magnetic field. N40 and N48 magnets were put under the cages and desired field intensities were established by controlling the magnets position, using a Gaussmeter (475 DSP Gaussmeter, Lake Shore cryotronics, Westerville, USA) to measure the intensities in each cage. Based on the results of the *in vitro* evaluation, the field intensity selected for the *in vivo* investigation was 155 mT ± 10. The tissue regeneration was evaluated after 1, 3, and 6 weeks from the surgery. In clinic, the timing of post-operative evaluation, particularly at 6 weeks, plays a crucial role in determining the outcomes of tendon surgical repair. Research indicates that early assessment can significantly influence recovery trajectories and long-term functional results. In particular, early improvement at 6 weeks results predictive of greater final improvement and patient satisfaction after 1 year. On the contrary, patients showing no improvement after 6 weeks are less likely to achieve significant recovery later, indicating the importance of early evaluation [36].

2.10.2. Histological analysis

As described in a previous work [28], the tissue samples were immediately immersed in 4 % v/v neutral buffered formalin and embedded in paraffin. One group of samples was stained with hematoxylin-eosin (H&E), whereas the other with picrosirius red (PSR). In order to apply PSR deparaffinized sections were hydrated, stained with Weigert's hematoxylin for nuclei, and afterwards stained with PSR for 1 h. After the staining, the sections were observed using a light microscope (Carl Zeiss Axiophot) and imaged (Nikon DS-Fi2).

2.11. Statistical analysis

Statistical analyses were performed using Astatsa statistical calculator. One-way analysis of variance (ANOVA) was followed by Scheffé for post-hoc comparisons. $p < 0.05$ was considered significant.

3. Results and discussion

3.1. Scaffolds chemico-physical characterization

A pre-formulative study was performed. The threshold concentration required to allow the generation of polymeric fibers is 8 % w/w. However, 20 % w/w is the minimum concentration to obtain the formation of regular and homogenous fine fibers without defects. Fig. 1 reports the SEM micrographs of the pre-formulative study fibers (P8, P20 and P30). The PHB concentration affects the fibers morphology: the lowest concentration (8 % w/w) leads to the production of a poor quantity of big and rigid fibers, while the highest concentration (30 % w/w) produces fibers with a high presence of beads and knots. The optimal concentration results the 20 % w/w, which allows to obtain a regular production of homogeneous fibers without defects.

As the P20 blend allows to obtain fibers with the best morphological characteristics, it was selected for the scaffolds' development. In order to improve the scaffolds mechanical properties, the cord scaffolds were combined creating a more complex-structured braid scaffold, as shown in Fig. 2a.

The scaffolds maintain their morphological characteristics in the micro-scale, with an aligned conformation which mimics the hierarchical structure of the tendon collagen fascicles. On the other side, the new more complex morphology on the macro-scale should increase the scaffold mechanical properties and should result in an easier handling during the surgical implant. As shown in Fig. 2b, the mechanical properties evaluation confirms that the braid structure is effective to increase the mechanical properties, in both dry and hydrated state and in terms of both maximum force at break (Fmax), elongation %, and Young's modulus (YM).

Due to the effectiveness of the braid conformation, the scaffold was developed with this particular shape and enriched with MNPs and Gel, in order to promote the cell adhesion and proliferation, and also to induce the cells mechano-stimulation [10].

A cytotoxicity test was performed in order to evaluate Fe_3O_4 cytotoxicity and determine the adequate amount of NPs to be loaded into the scaffolds without causing a toxic effect. Two different types of NPs were tested: with (Fe_3O_4@OA) and without (Fe_3O_4) an oleic acid coating. Results demonstrate that the NPs coated with oleic acid are characterized by a cell growth superimposable to that of the positive control, meaning that they do not cause any toxic effect on the cells (Supporting Information: Fig. S6). Based on this, Fe_3O_4@OA NPs were selected and added at the final polymeric blend at the concentration of 2 mg/mL.

The final scaffolds, namely P20, P20-Fe_3O_4, and P20-Fe_3O_4-Gel, were developed and characterized for their morphology, fibers dimensions, and wettability, as shown in Fig. 3.

Fig. 3a shows the SEM micrographs of the obtained fibers as spun and after 1 week of hydration. It is possible to observe that all the fibers are characterized by a smooth surface and an aligned conformation that should mimic the tendon fascicles. More importantly, the fibers containing gelatin are characterized by a significantly higher swelling than P20 and P20-Fe_3O_4. This indicates that the Gel is effective in increasing the scaffolds capability to adsorb water, which should result in a more favorable surface for the cell adhesion.

Moreover, the identification of Fe_3O_4@OA NPs into the fibrous matrix was studied using SEM-EDX. Fig. 3b reports the micrographs with the corresponding EDX spectra, which underline the presence of Fe_3O_4@OA embedded into the fibers, represented by the white particles detected in the micrographs. On the contrary, it is noticeable that no

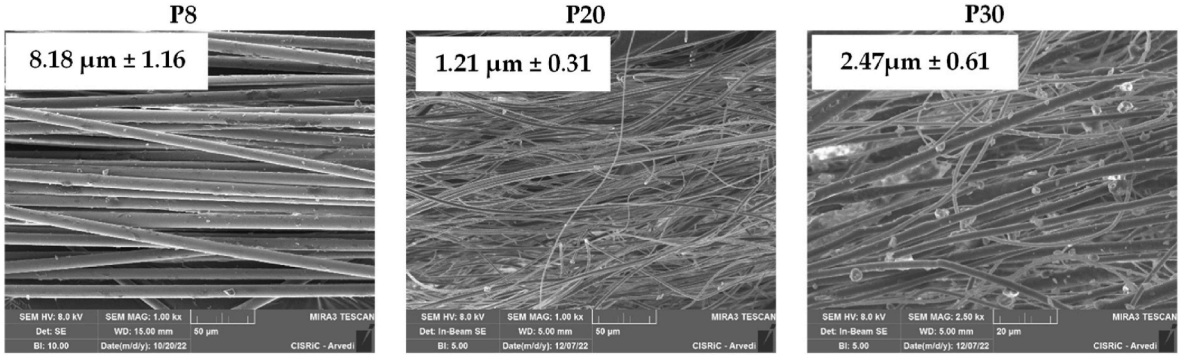

Fig. 1. SEM micrographs of centrifugal spun fibers based on P8, P20, and P30 blends. In the insets, the corresponding dimensional analysis is reported (mean values ± s.d.; n = 90).

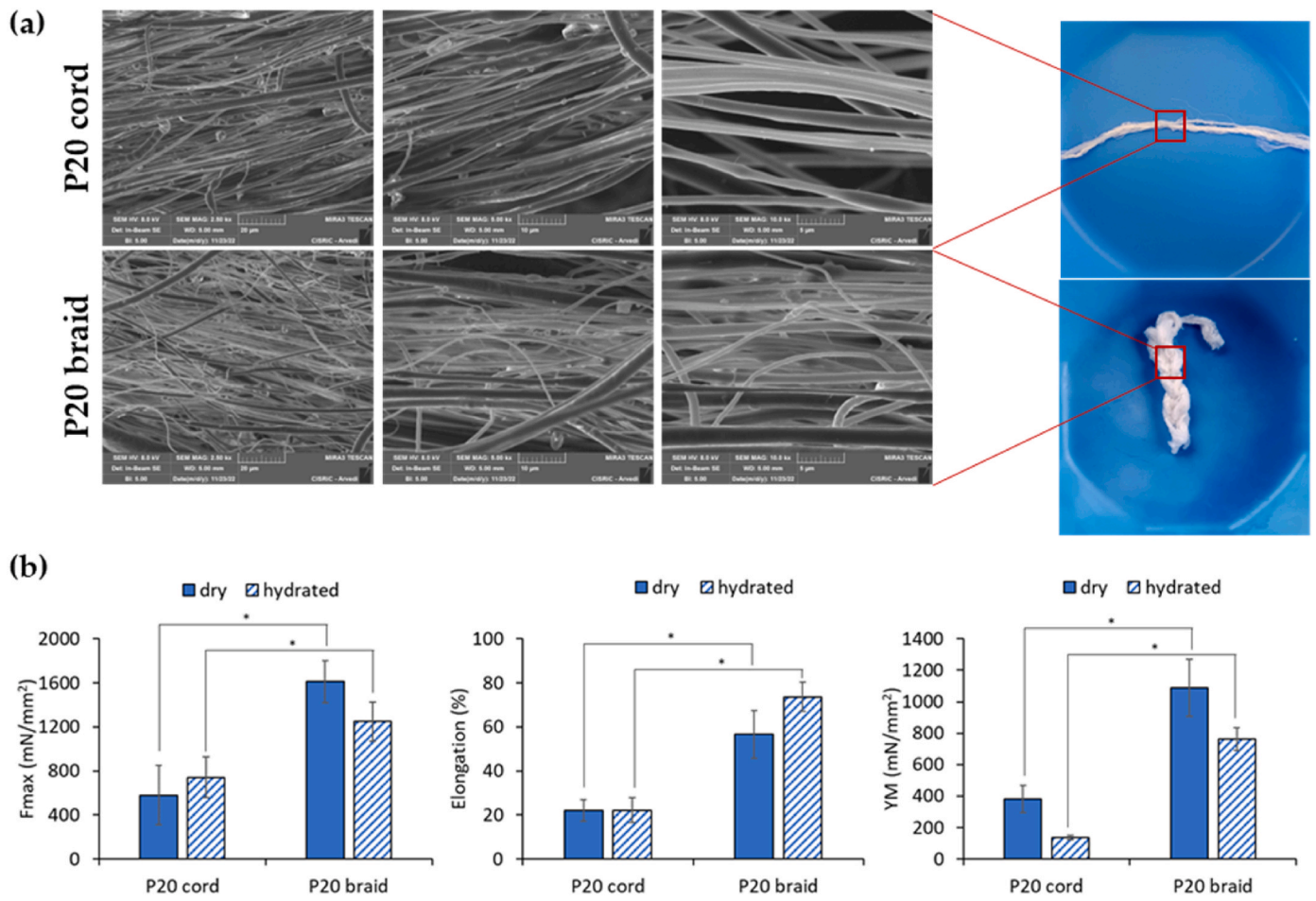

Fig. 2. (a) SEM micrographs of centrifugal spun fibers based on P20 blend in cord (upper line) and braid (lower line) conformation, with the corresponding images; (b) Mechanical properties of the P20 cord scaffold compared with the P20 braid scaffold in dry and hydrated state (mean values ± sd; n = 4). ANOVA one-way; Scheffé test ($p \leq 0.05$). * indicates statistical differences.

trace of Fe is detected into the P20 fibers.

Afterwards, the interfacial properties of the scaffolds and their hydrophilicity and wettability were evaluated using contact angle measurements. Fig. 3c reports the shape, and the contact angle values for a 0.1 μL buffer drop released onto the scaffolds for 1s and 3s.

It is evident that the presence of Gel regulates the surface wettability. In fact, P20 and P20-Fe_3O_4 scaffolds are characterized by a similar hydrophobicity (123° and 114° respectively), which do not change after 3s of contact between the droplet and the surface. On the other hand, the P20-Fe_3O_4-Gel scaffold after 3s of contact is characterized by a significant increase in the surface wettability, reaching a value of 89.9°, which could be considered a hydrophilic surface since it is less than 90° [37]. This indicates the effectiveness of the Gel loading into increasing the surface wettability.

3.2. Magnetic characterization

Recent advances showed that the combination of scaffolds and MNPs could result in unique properties to control cell signalling. In particular, the magnetic force stimulation resulted effective in regulating the inflammatory response in tendon treatment [38], and also in promoting the tenogenic differentiation of stem cells thanks to the mechanical force that it generates [39]. More importantly, scaffolds enriched with MNPs could lead to the cells mechano-stimulation, fundamental for the tendon tissue regeneration. In fact, when a magnetic field is applied, the scaffolds could respond with vibrations generating a transient physical force that could be transferred to the host cells [16]. One important aspect is also represented by the superparamagnetic behavior of Fe_3O_4 NPs with diameters of less than 20 nm, which is of particular interest as they lose magnetism once the field is removed allowing a precise remote control over their functions [10,40]. In fact, the MNPs superparamagnetic characteristics present numerous applications in tissue repair and regeneration, particularly in enhancing therapeutic strategies. These nanoparticles can be manipulated using magnetic fields, allowing for precise control over cellular behavior and tissue formation. In particular, MNPs have been shown to facilitate the guided migration and differentiation of stem cells into specific cell types, by modifying the cellular microenvironment. Moreover, they enable the formation of structured cell assemblies and multicellular clusters, which are essential for creating three-dimensional tissue constructs [41]. MNPs also seem to play a role in controlling inflammation and reducing scar formation, which are critical for effective tissue healing [42].

The magnetic properties of the scaffolds enriched with Fe_3O_4@OA NPs were evaluated by SQUID measurements (Fig. 4).

The M vs μ_0H curves (where M represent the magnetization and μ_0H the external magnetic field) indicate the typical magnetic behavior of magnetite NPs (Fig. 4a). In fact, they show a superparamagnetic behavior at 300 K as there is no hysteresis loop after the application of the magnetic field, due to the fact that every crystal of the NPs acts as a single magnetic domain. On the other hand, the scaffolds show a ferrimagnetic behavior at 5 K, since a hysteresis loop is clearly visible in the M vs μ_0H curves, meaning that the magnetic moments stay aligned even in the absence of the external stimulation of a magnetic field [43]. These results confirm that, after their incorporation into the P20 and P20-Gel

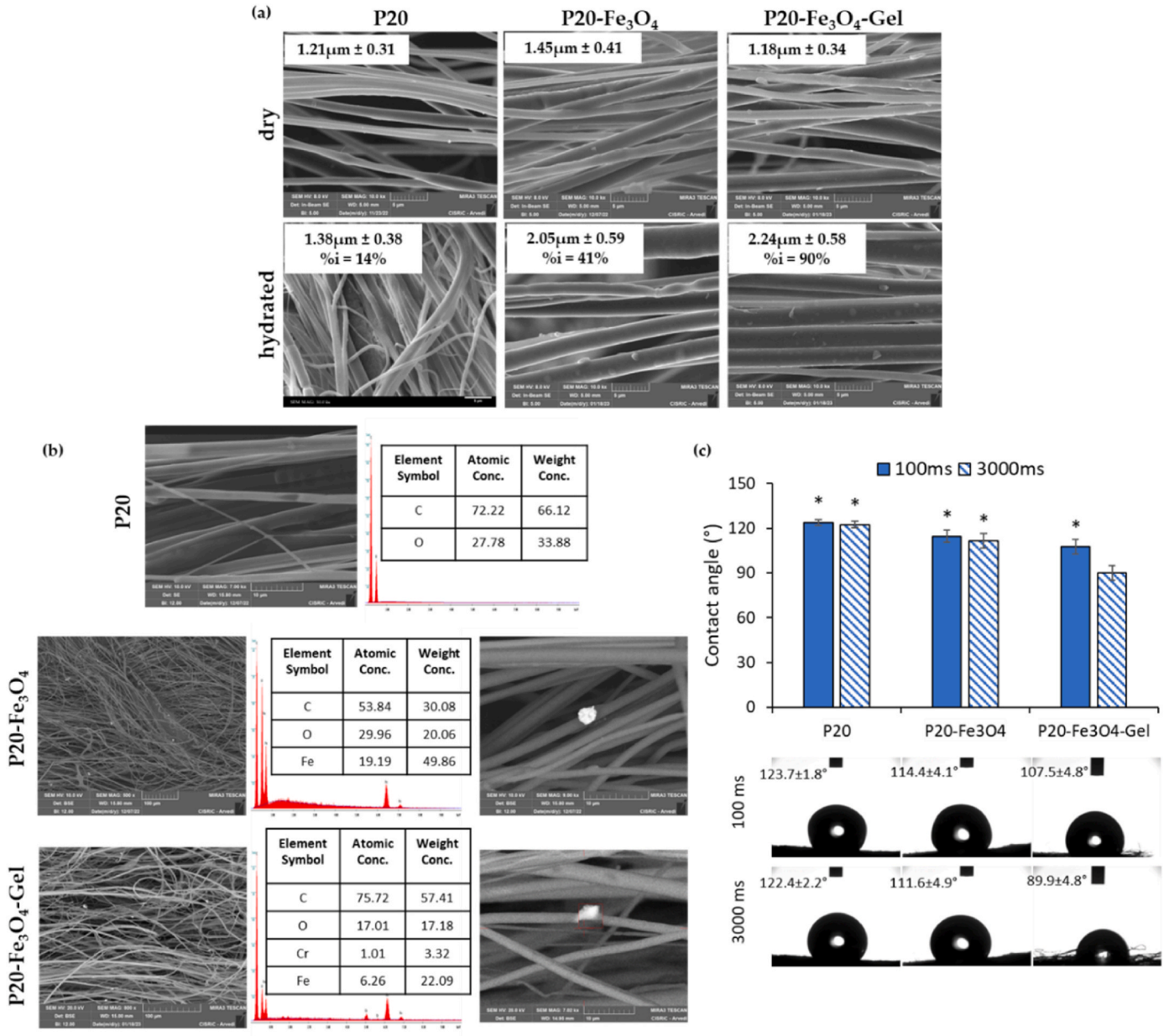

Fig. 3. (a) SEM micrographs of P20, P20-Fe_3O_4, and P20-Fe_3O_4-Gel scaffolds in dry state and after 1 week of hydration in water at 10.0kx magnification (scale bar: 5 μm). In the insets, the corresponding dimensional analysis is reported together with the percentage of fibers increase after hydration (%i) (mean values ± sd; n = 30); (b) SEM-EDX of P20, P20-Fe_3O_4, and P20-Fe_3O_4-Gel scaffolds with the corresponding spectra (left panel scale bar: 100 μm; right panel scale bar: 10 μm). The white particles represent the detected Fe_3O_4@OA NPs; (c) Contact angle measurements of the P20, P20-Fe_3O_4, and P20-Fe_3O_4-Gel scaffolds evaluated after 100 ms and 3000 ms of contact between the droplet and the surface (mean values ± sd; n = 4). ANOVA one-way; Scheffé test ($p \leq 0.05$). * indicates statistical differences with P20-Fe_3O_4-Gel 3000 ms.

matrices, the NPs maintain the superparamagnetic characteristics, indicating that the polymers do not influence their intrinsic behavior.

The ZFC-FC (Zero Field Cooled - Field Cooled) curves of the magnetization indicate the size of the Fe_3O_4@OA NPs (Fig. 4a, right panel). These curves are typical of relatively large NPs (around 20–30 nm). Since the loaded NPs should have a diameter of 10 nm, these results could indicate that small particle clusters are present in the polymeric matrix. This could be also confirmed by the SEM-EDX analysis (Fig. 3b), which shows the presence of particle clusters within the fibers. Furthermore, the ZFC-FC curve allows to calculate the % of Fe_3O_4@OA NPs effectively embedded into the scaffolds (Table 2). Both P20-Fe_3O_4 and P20-Fe_3O_4-Gel scaffolds have an effective % of embedded NPs similar to the theoretical one, indicating the effectiveness of the manufacturing process. This could be also confirmed by the comparison of the scaffolds' M vs μ_0H curves (Fig. 4b) which almost overlap. This means that they have similar magnetism and therefore the NPs have been incorporated in the same amount.

As a proof of concept, scaffolds containing an increasing quantity of Fe_3O_4@OA NPs were also evaluated for their magnetism (Supporting Information: Fig. S7). A constant increase in the moment directly related to the magnetite concentration is clearly visible in all the curves. Moreover, the calculation of the % of Fe_3O_4@OA NPs effectively embedded into the scaffolds (Supporting Information: Table S1) also in this case demonstrates that the concentration of NPs effectively embedded into the scaffolds is similar to the theoretical one, ulteriorly confirming the effectiveness of the manufacturing process.

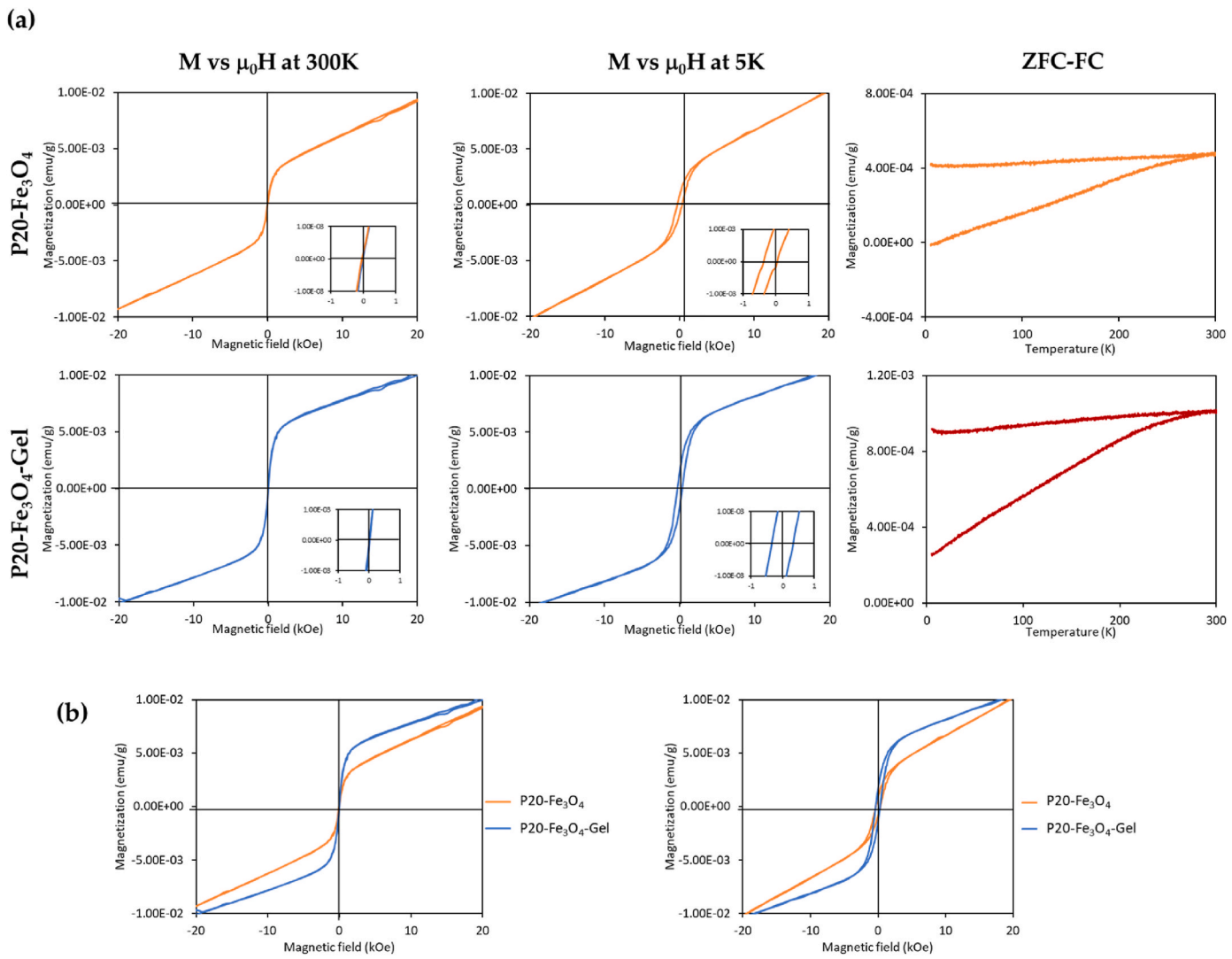

Fig. 4. (a) SQUID measurements M vs μ_0H at 300K, and 5K, and ZFC-FC curves of the scaffolds; (b) comparison of the M vs μ_0H at 300K (left panel) and M vs μ_0H at 5K (right panel) curves of the scaffolds.

Table 2
% Fe_3O_4@OA NPs effectively incorporated into the scaffolds.

Scaffold	% Fe_3O_4@OA NPs incorporated	% theoretical
P20-Fe_3O_4	0.23	0.20
P20-Fe_3O_4-Gel	0.29	0.20

3.3. Structural characterization

The scaffolds were studied by means of infrared spectroscopy and thermal analysis. Fig. 5a reports the FTIR profiles of the scaffolds compared to the raw materials, Fig. 5b reports the TGA analysis, and Fig. 5c reports the DSC analysis.

The FTIR spectrum of Fe_3O_4@OA NPS shows characteristics peaks at 580 cm^{-1} (peak 1) related to the Fe–O stretching vibration [38]. The same peaks are present in the P20-Fe_3O_4 and P20-Fe_3O_4-Gel spectra with lower intensity. This could suggest that the NPs are embedded into the polymeric matrix. Moreover, the bands near 1300 cm^{-1} (peak 2) and 3400 cm^{-1} (peak 3) are related to the O–H stretching vibration of the Fe_3O_4@OA NPs [43,44]. As it concerns the Gel spectrum, the band near 1330 cm^{-1} (peak 4) is related to the vibration of the proline side chains, whereas the peaks between 1100 cm^{-1} (peak 5) and 1460 cm^{-1} (peak 6) could be attributed to the presence of type I Gel. Moreover, a peak related to the amide I C=O stretching at 1640 cm^{-1} and a peak related to the amide II N–H deformation at 1500 cm^{-1} (peak 7) are present in the P20-Fe_3O_4-Gel scaffold [45].

The TGA and DSC spectra are mainly typical of the PHB, since it is the main component of the scaffolds. However, the TGA confirms the incorporation of the Fe_3O_4@OA, since the plateau performed at 900 °C for 30 min leaves the inorganic components. On the other hand, this is not present in the P20 scaffold spectrum, where the matrix is completely burned.

As a general trend, all the scaffolds independently of their composition are stable until 250 °C, also confirming that the manufacturing process is compatible with the material properties. From this point, they start showing a fast and intense weight loss until 300 °C, with the exception of the P20-Fe_3O_4-Gel, which keeps on losing weight until 450 °C due to the presence of Gel.

The architecture of scaffolds at the nanoscale was investigated by SAXS. Fig. 5d reports the SAXS spectra of the scaffolds (right panel) and of the Fe_3O_4@OA NPs (left panel). The spectra show the characteristic features of a polymer matrix at the nanoscale. A broad peak is present in all systems at $q = 1.15\ nm^{-1}$, corresponding to a characteristic polymer chain distance of 5.5 nm inside the PHB matrix, preserved in the presence of 20 % relative w/w Gel. At low-q, corresponding to distances of the order of the hundreds of nms, the scattered intensity of the hydrated

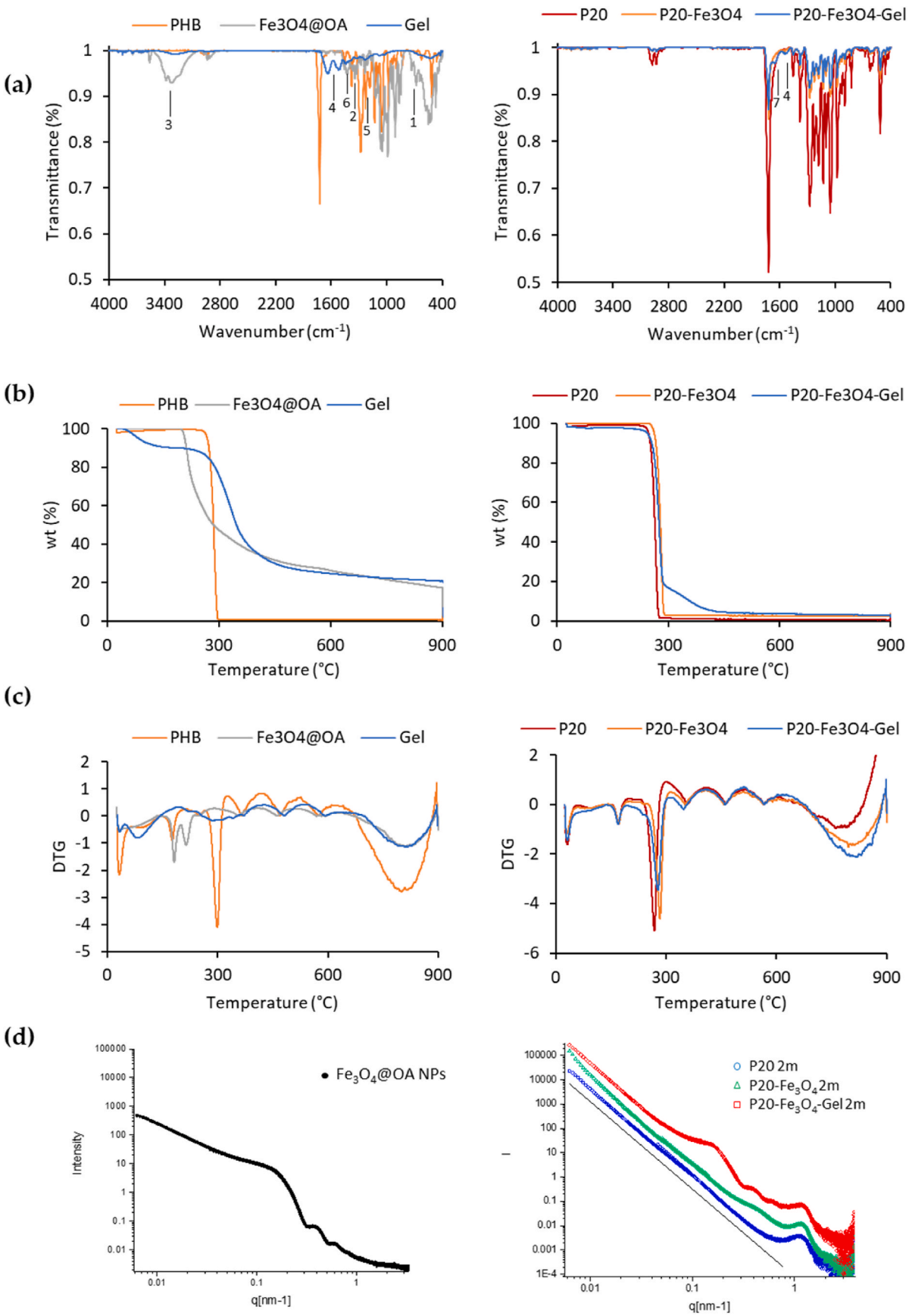

Fig. 5. (a) FTIR spectra of the scaffolds (right column) and of the raw materials (left column); (b) TGA analysis of the scaffolds (right column) and of the raw materials (left column); (c) DSC analysis of the scaffolds (right column) and of the raw materials (left column); (d) SAXS spectra of the Fe_3O_4@OA NPs (left panle) and of the scaffolds (right panel) vertically shifted for better visibility. Black line represents the trend of the I(q) decay.

scaffolds follows a I(q) ÷ $q^{-3.6}$ decay, revealing a surface fractal arrangement of the fibers, with compact internal packing and moderate surface roughness.

In the central region, the presence of Fe_3O_4@OA NPs is clearly visible in the two loaded samples. The spectrum of Fe_3O_4@OA NPs is reported for comparison. The NPs are partially clusterized in aggregates, that can be anyway embedded in the scaffolds, as already suggested by the SEM-EDX (Fig. 3b).

3.4. Mechanical properties evaluation

Fig. 6a reports the mechanical properties evaluation (Fmax, elongation %, and YM) performed on the scaffolds in both dry and hydrated state. All the systems display different mechanical properties in the dry and hydrated state. The higher elongations at break, induced by lower Fmax, reveal that the hydrated scaffolds are more ductile with a more extended plastic regime. Also, they are less rigid, showing a lower YM in the elastic regime. The presence of Fe_3O_4@OA into the matrix seems to affect the mechanical properties of the scaffolds. Both a decrease of the elongation and Fmax at break are visible, suggesting a lower ductility or higher fragility. The mechanical properties could be influenced by the presence and the distribution of the Fe_3O_4@OA NPs into the fibrous matrix. In fact, they may have reduced the flexibility of the scaffolds by decreasing the free volume between the polymer chains and, consequently, their mobility [46]. In the elastic regime the scaffolds with Fe_3O_4@OA show a higher YM than P20 in the dry state, corresponding to a higher rigidity, while displaying a similar elastic behavior upon hydration. The mechanical properties of human tendons greatly vary according to their location, with an ultimate tensile strength that ranges from 5 to 100 MPa and a strain of failure between 10 and 15 % [47]. The developed scaffolds could not sustain a complete tissue breakage. However, they could successfully mimic the elastic regime of tendons,

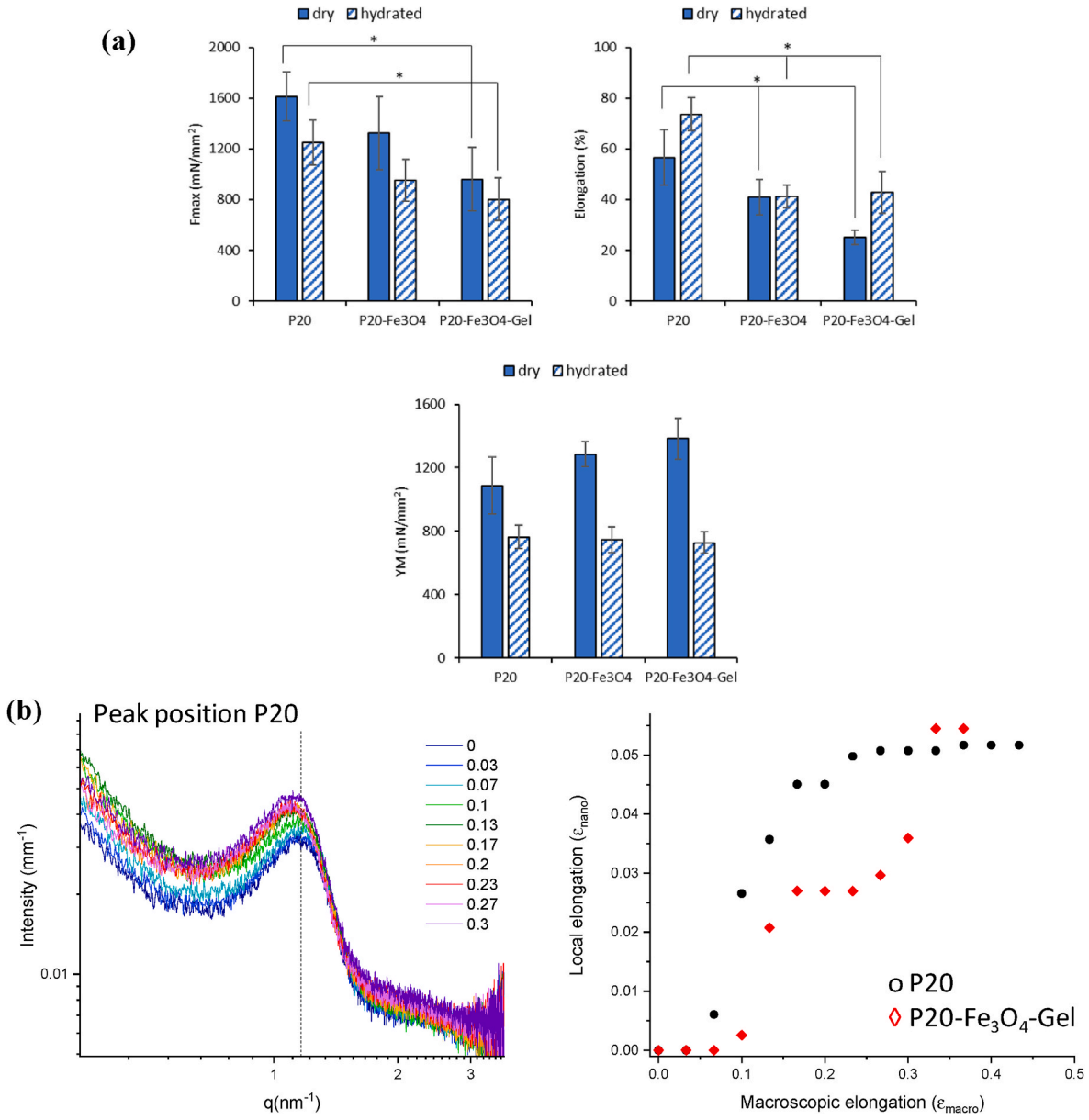

Fig. 6. (a) Mechanical properties of the P20, P20-Fe_3O_4, and P20-Fe_3O_4-Gel scaffolds in dry and hydrated state (mean values ± s.d.; n = 4). ANOVA one-way; Scheffé test ($p \leq 0.05$). * indicates statistical differences between the results; (b) SAXS intensity profiles of P20 scaffolds in the region of the characteristic peak at increasing macroscopic elongation. The calculated values for the local elongation (ε_{nano}) are reported as a function of the macroscopic elongation (ε_{macro}) for P20 (black) and P20-Fe_3O_4-Gel scaffolds (red). (For interpretation of the references to colour in this figure legend, the reader is referred to the Web version of this article.)

supporting a 15 % elongation (the strain of failure of native tendons) without breaking. This could guarantee the structural support of a partial breakage, where it is fundamental for the host cells to find a pattern that mimic the native ECM, consequently stimulating a more rapid regeneration of the tissue. Finally, the tendon stiffness greatly influences the YM *in vivo*. Similarly, the YM of the developed scaffolds could be modulated by increasing or reducing their stiffness in order to adapt the corresponding YM to the one required.

The macroscopic mechanical properties were correlated with the nanoscopic mechanics of the polymer matrix. The evolution of the nanoscale structure while the scaffolds were subjected to elongation, were observed acquiring the scattered X-ray 2D patterns at several consecutive strain increments $\Delta l = 0.5$ mm, corresponding to an elongation ε_{macro} of 3.3 %. Fig. S8 reports the 2D patterns collected for the different PHB-based samples in hydrated conditions at 0 % and 25 % elongation. At 25 % elongation, patterns are asymmetric, with a shrinkage along the direction of the tension. The contraction observed in the direction of the fibre axis in the 2D patterns indicates an elongation of the internal structure of the polymer matrix in the direction of tension. The analysis of the scattered intensity profiles at increasing elongation was performed by observing the shift of the characteristic structure peak at $q = 1.15$ nm^{-1}, as reported in Fig. 6b (left panel). The displacement of the peak towards lower q-values indicates an increase in the characteristic distance between polymer chains (from the initial $d = 5.5$ nm) within the polymeric matrix. The local elongation ε_{nano} was calculated and reported as a function of the macroscopic elongation ε_{macro} in Fig. 6b (right panel) for P20 and P20-Fe_3O_4-Gel scaffolds. P20-Fe_3O_4 results are similar to the ones of P20-Fe_3O_4-Gel system. Notably, the nano-scale strain is significantly smaller than the macroscopic strain along the loading direction. Results indicate that the polymer PHB matrix does not simply deform under tension, but rearranges itself, deforming locally less than expected. The ratio between the two

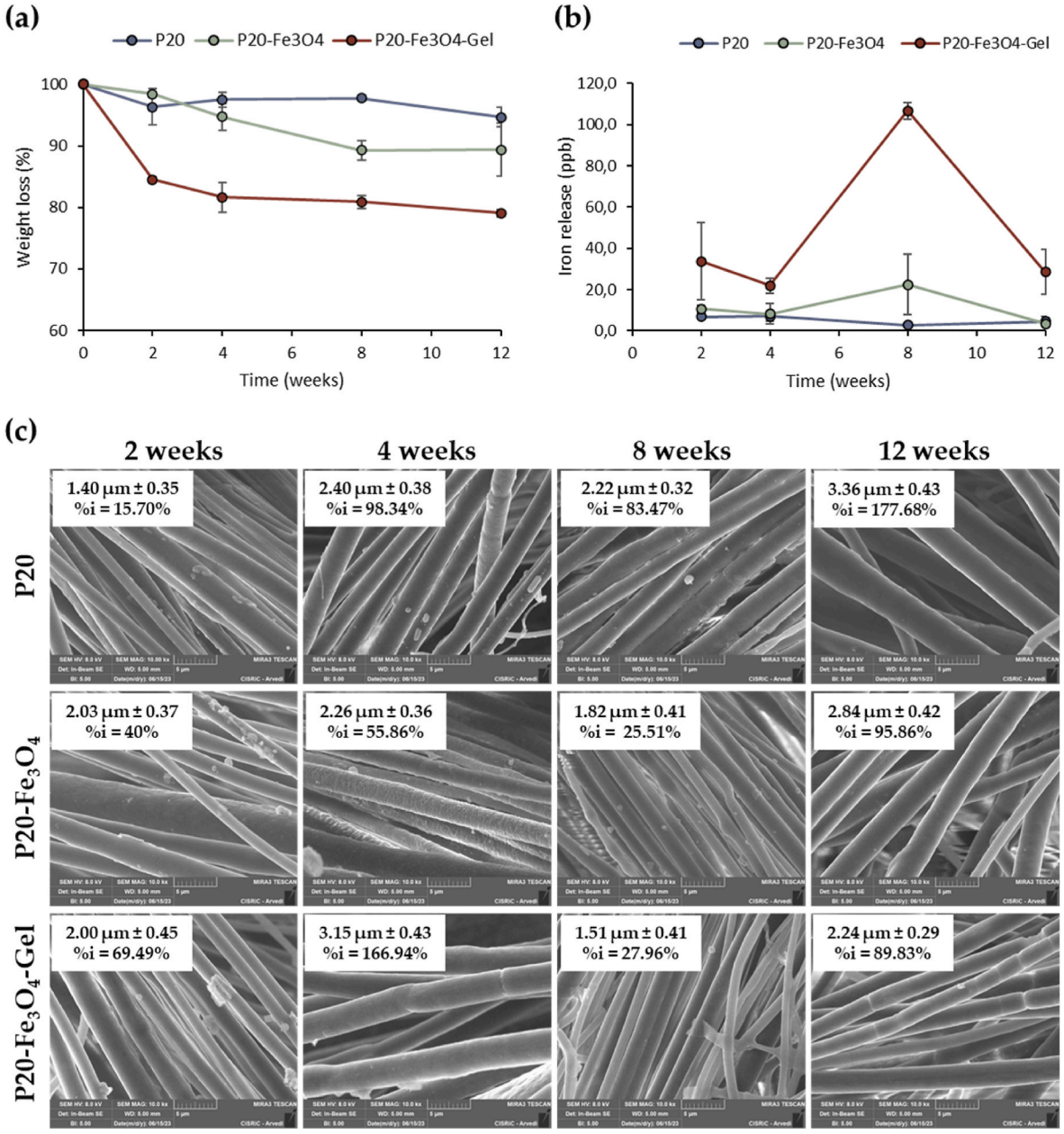

Fig. 7. (a) Weight loss (%) evaluated for the scaffolds after 2, 4, 8, and 12 weeks of degradation (mean values ± s.d.; n = 3); (b) Fe^{2+}/Fe^{3+} released from the scaffolds after 2, 4, 8, and 12 weeks of degradation (mean values ± s.d.; n = 3); (c) SEM micrographs of the scaffolds at different times of degradation at 10.0kx magnification (scale bar: 5 µm). In the insets, mean fibers diameters and % of fibers increase (%i) upon degradation are reported (mean values ± s.d.; n = 90).

elongations ($\varepsilon_{nano}/\varepsilon_{macro}$) is ¼ for PHB up to 20 % macroscopic elongation. At higher macroscopic strains, a plateau in the local structure is observed until the breakpoint. The peculiar behaviour is enhanced by the presence of Fe_3O_4@OA NPs and gelatin, as visible in Fig. 6b (right panel). The ratio between the two elongations ($\varepsilon_{nano}/\varepsilon_{macro}$) is about 1/6 up to 20 % macroscopic elongation and the limit local deformation is reached at higher strains ($\varepsilon_{macro} > 30$ %), close to the breakpoint.

During SAXS acquisitions, the forces necessary to keep the imposed values of strain were measured. At each elongation increment, $\Delta l = 0.5$ mm, a time evolution of the force was observed, indicating a stress relaxation process in all the systems. Results are reported in Fig. S9, confirming the viscoelastic behaviour of the scaffolds under tension, as expected for polymer networks. The presence of gelatin seems to increase the relative importance of the viscous contribution to the mechanical behaviour of the P20-Fe_3O_4-Gel scaffolds.

3.5. Scaffolds in vitro degradation and Fe_3O_4@OA release

The degradation was investigated *in vitro* in PSB to simulate the pH and ionic strength of aqueous environment, site of scaffold implant. Fig. 7a reports the scaffolds *in vitro* degradation, whereas Fig. 7b reports the Fe^{2+}/Fe^{3+} release during the degradation, and Fig. 7c shows the SEM micrographs of the scaffolds at different degradation times (2, 4, 8, and 12 weeks) with the corresponding dimensional analysis.

It is noticeable that the scaffold with Gel is characterized by a strong weight loss of about 20 % during the first month and then it reaches a plateau, while the scaffold of just PHB is stable and characterized by a low weight loss of about 6 % in 3 months. This is probably due to the loss of the Gel, which could remain for the time needed to allow the cell attachment and initial proliferation, and then degrade leaving the strong structure of the PHB as a support. The P20-Fe_3O_4 scaffold also shows a slight degradation of about 10 % in 12 weeks, that could be due to the loss of superficial magnetite NPs which were not embedded in the polymeric matrix.

During the degradation, the scaffolds are characterized by a low Fe^{2+}/Fe^{3+} loss, as shown in Fig. 7b. In fact, at every time interval the Fe^{2+}/Fe^{3+} detection is in the order of ppb, meaning that, in all cases, the Fe_3O_4@OA NPs are well integrated into the polymeric matrix. In particular, the iron loss in 12 weeks was less than 0.05 % of the total MNPs amount, suggesting that iron ions therapeutic effect could be considered not significant. Interestingly, the P20-Fe_3O_4-Gel scaffold is characterized by a higher Fe^{2+}/Fe^{3+} loss after 8 weeks, which is probably related to the faster degradation of Gel and the cosequent loss of more superficial NPs. However, in all cases Fe^{2+}/Fe^{3+} is neglegible (<0.05 % w/w of the total MNPs amount) suggesting that Fe_3O_4@OA NPs are firmly entrapped into the polymeric matrix that completely surrounds them, and the released amount is probably related to the residues present on the fibers' surface.

However, the scaffolds maintained their integrity in terms of morphology and fibers orientation after 3 months of degradation, showing an increase in the surface roughness and a linear increase in the fibers dimensions (Fig. 7c). Interestingly, the P20-Fe_3O_4-Gel scaffold is characterized by a significantly higher fiber swelling after 4 weeks of degradation, while the same parameter decraeses after 8 weeks. This could ulteriorly confirm the weight loss results showed in Fig. 7a. In fact, the Gel could lead to an increase in the water adsorption during the first month, while after its degradation it could leave the PHB skeleton, which needs to be re-hydrated.

3.6. Cell proliferation assay

The application of external magnetic fields on cells was proven to improve cells migration, homing efficiency, and differentiation potential, having beneficial effects in therapeutic applications [48,49]. Since this field was widely explored in literature, this research mainly aimed at the investigation of the potential synergic effect of magnetic field and ECM-like scaffolds, to improve the rehabilitation capability in respect to the results reported in literature on scaffolds or magnetic fields alone. Starting from this statement, the cell proliferation due to the combination between MNPs-enriched scaffolds and external magnetic stimulation is here reported (Fig. 8a). The test was performed on the scaffolds with and without the application of different magnetic fields for 21 days. It is clearly visible that after 3 days of growth the higher fields (155 and 285 mT) seem effective on the cell growth when combined with the scaffolds enriched with magnetite. On the other hand, the control of cells grown in standard conditions (GM) and the P20 scaffold are characterized by a cell proliferation that is similar with and without the application of the magnetic field.

Moreover, the Gel seems also effective since the cells are able to grow better in respect to the other scaffolds. The same trend is observed after 7, 14, and 21 days, with the P20-Fe_3O_4-Gel scaffold having the best performance. In particular, after 21 days the cells growth onto the P20-Fe_3O_4-Gel scaffold with the application of the magnetic fields reaches values considerably higher than that of the GM and the P20 scaffold.

More importantly, the CLSM images (Fig. 8b) and the SEM micrographs (Fig. 8c) confirm the effectiveness of the combination of the scaffolds and the application of an external magnetic field also on the cells' alignment. It is clearly visible that the cells are randomly oriented when no external magnetic field is applied on the scaffolds loaded with Fe_3O_4@OA NPs, and they always appear randomly oriented onto the P20 scaffold. On the other hand, when the magnetic field is applied onto the P20-Fe_3O_4 and P20-Fe_3O_4-Gel scaffolds (especially the higher fields of 155 and 285 mT) the cells assume an elongated shape and they appear aligned onto the matrix. Moreover, the Gel is also effective on the cell adhesion, since the P20-Fe_3O_4-Gel is characterized by a higher attachment than the other scaffolds after 21 days.

The same trend is observed with hASCs (Fig. 8d). In fact, after 21 days of culture, the hASCs seeded onto the P20-Fe_3O_4-Gel scaffold together with the application of the higher magnetic fields (155 and 285 mT) show a growth significantly higher than the ones grown without the magnetic stimulation. Moreover, even in this case the cells grown in GM and the P20 scaffold are characterized by a cell proliferation that is similar with and without the application of the magnetic field. More importantly, the CLSM images (Fig. 8e) show that hASCs are able to differentiate and produce collagen I matrix when the NPs-doped scaffolds are combined with an external magnetic stimulation. In fact, the cells result elongated onto the scaffolds and a green signal corresponding to collagen I is visible in the cells proximity. This is probably due to the magnetic stimulation, which seems to upregulate the expression of tendon-associated genes, as mentioned also in previous studies [38,39]. Research works indicate that mechanical loading via magnetic stimulation can repress matrix-degrading enzymes like matrix metalloproteinase-3 (MMP-3), which is crucial for maintaining tendon matrix integrity [50] Moreover, exposure to low-frequency static magnetic fields has been shown to influence cytoskeletal organization, which is linked to enhanced mechanosensing and gene expression in stem cells, further supporting tenogenesis [16]. In fact, this can lead to significant upregulation of genes such as scleraxis (SCX), Collagen Type I Alpha 1 (COL1A1), and Tenascin C (TNC) in tendon-derived cells, enhancing their regenerative potential [38]. Finally, as already mentioned, magnetic stimulation seems able to modulate inflammatory cytokines, favoring a pro-regenerative environment beneficial for tendon healing [51].

On the other hand, the cells grown onto P20 scaffold maintain hASCs' phenotype, and no green signal is visible.

From these results, it is possible to conclude that the superparamagnetic Fe_3O_4@OA NPs embedded into the polymeric scaffolds and the static magnetic field acted synergically to stimulate the cell adhesion and proliferation.

As already mentioned, the supposed mechanism is mechano-stimulation. In fact, the nano-movements induced by the magnetic field on the scaffolds seem able to stimulate cells proliferation,

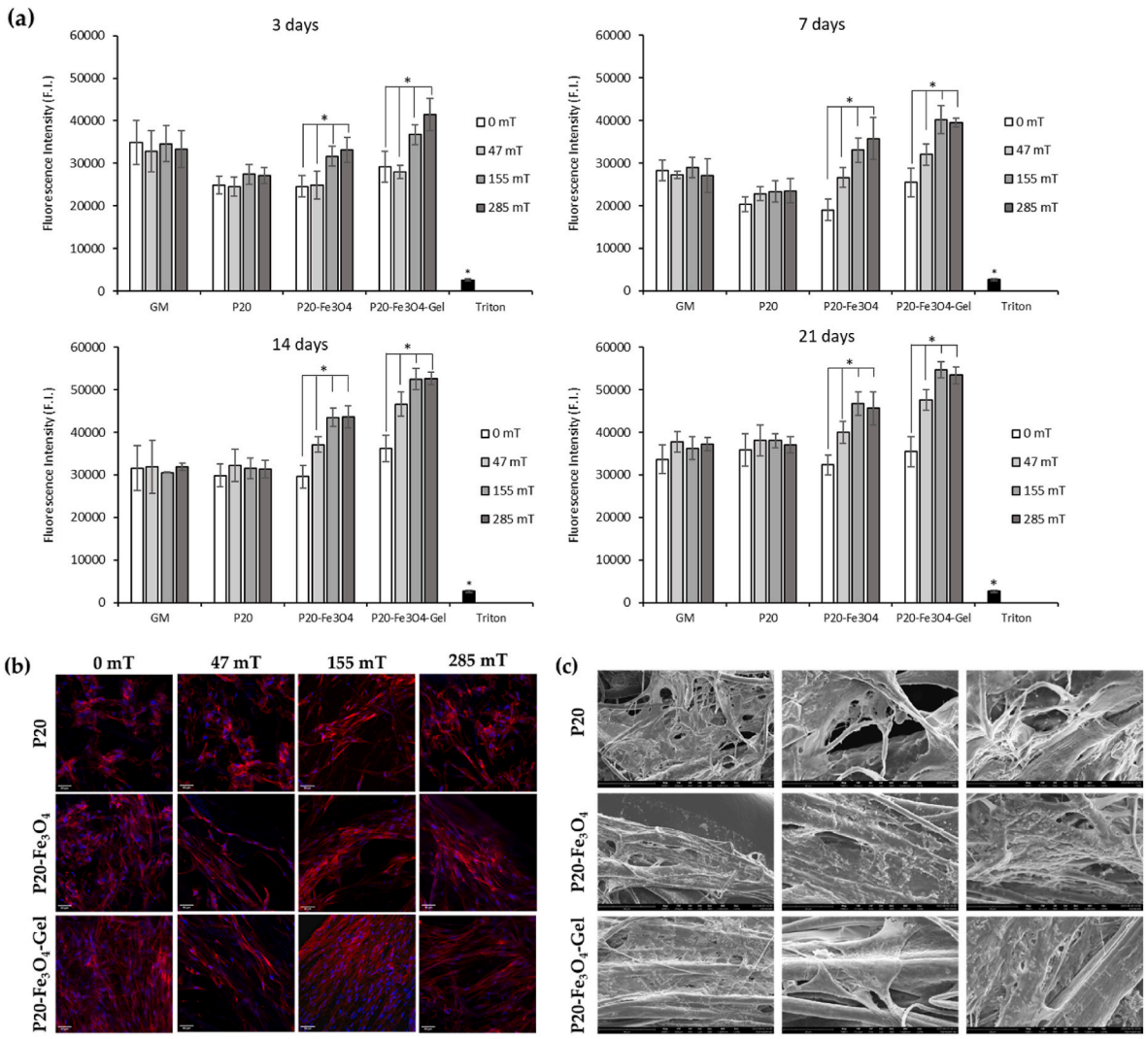

Fig. 8. (a) Aqua Bluer assay at 3, 7, 14, and 21 days of fibroblasts culture onto the scaffolds, with and without the application of different magnetic fields. Cells grown in standard conditions (GM) were used as a positive control and Triton 10 % v/v was used as negative control (mean values ± sd; n = 6). ANOVA one-way; Scheffé test ($p \leq 0.05$), * indicates statistical differences; (b) CLSM images of fibroblasts grown onto the scaffolds for 21 days with and without the application of different magnetic fields (nuclei stained in blue: DAPI; cytoskeletons stained in red: Phalloidin-TRITC) (scale bar: 50 μm); (c) SEM micrographs of fibroblasts grown onto the scaffolds for 21 days with the application of the 155 mT magnetic field; (d) Aqua Bluer assay at 3, 7, 14, and 21 days of hASCs culture onto the scaffolds, with and without the application of different magnetic fields (GM: positive control; Triton 10 % v/v: negative control) (mean values ± sd; n = 6). ANOVA one-way; Scheffé test ($p \leq 0.05$), * indicates statistical differences; (e) CLSM images of hASCs grown onto the scaffolds for 21 days with and without the application of different magnetic fields (nuclei stained in blue: DAPI; cytoskeletons stained in red: Phalloidin-TRITC; Collagen I matrix stained in green: ATTO 488 goat anti rabbit IgG) (scale bar: 50 μm). (For interpretation of the references to colour in this figure legend, the reader is referred to the Web version of this article.)

alignment, and differentiation, allowing deeper tissue reparation [10]. This stimulation primarily occurs through the interactions between cells and ECM, influencing cell behavior through various signaling pathways, primarily by modulating intracellular mechanisms and cellular responses. The modulation occurs via several key processes, including inflammatory responses and ion channel dynamics, which collectively contribute to the therapeutic effects observed in tissue regeneration [51]. In particular, the forces are transmitted via the integrin membrane protein, triggering a series of pathways that influence the cells behavior. The main route for mechanical force transmission within cells is through filamentous actin (F-actin), which plays a role in various processes such as adhesion, proliferation, and changes in morphology. When an external force is applied, the extracellular α-chain of integrin is activated, relaying the signal to the F-actin cytoskeleton, which induces internal contractility, consequently forming integrin-based focal adhesion complexes that connect with the ECM [52,53]. Additionally, membrane ion channels also serve as mechanosensitive sensors. Their molecular structure can change in response to mechanical stimuli, altering the membrane's permeability and influencing cell fate. In particular, G-protein-coupled receptors (GPCRs) are key ion channels that detect external forces, releasing signaling molecules that lead to the remodeling of the surrounding matrix. When exposed to mechanical stimuli, specific signals to the membrane proteins, like integrins and GPCRs, can regulate gene expression through various pathways, involving biochemical signals in the cytoplasm that are transmitted to the nucleus [54,55]. These lead to gene expression regulation and increased cell proliferation, consequently deepening tissue repair [56–58].

3.7. Pro-inflammatory immune response and hemolysis test

The interplay between inflammation and stem cell behavior is crucial

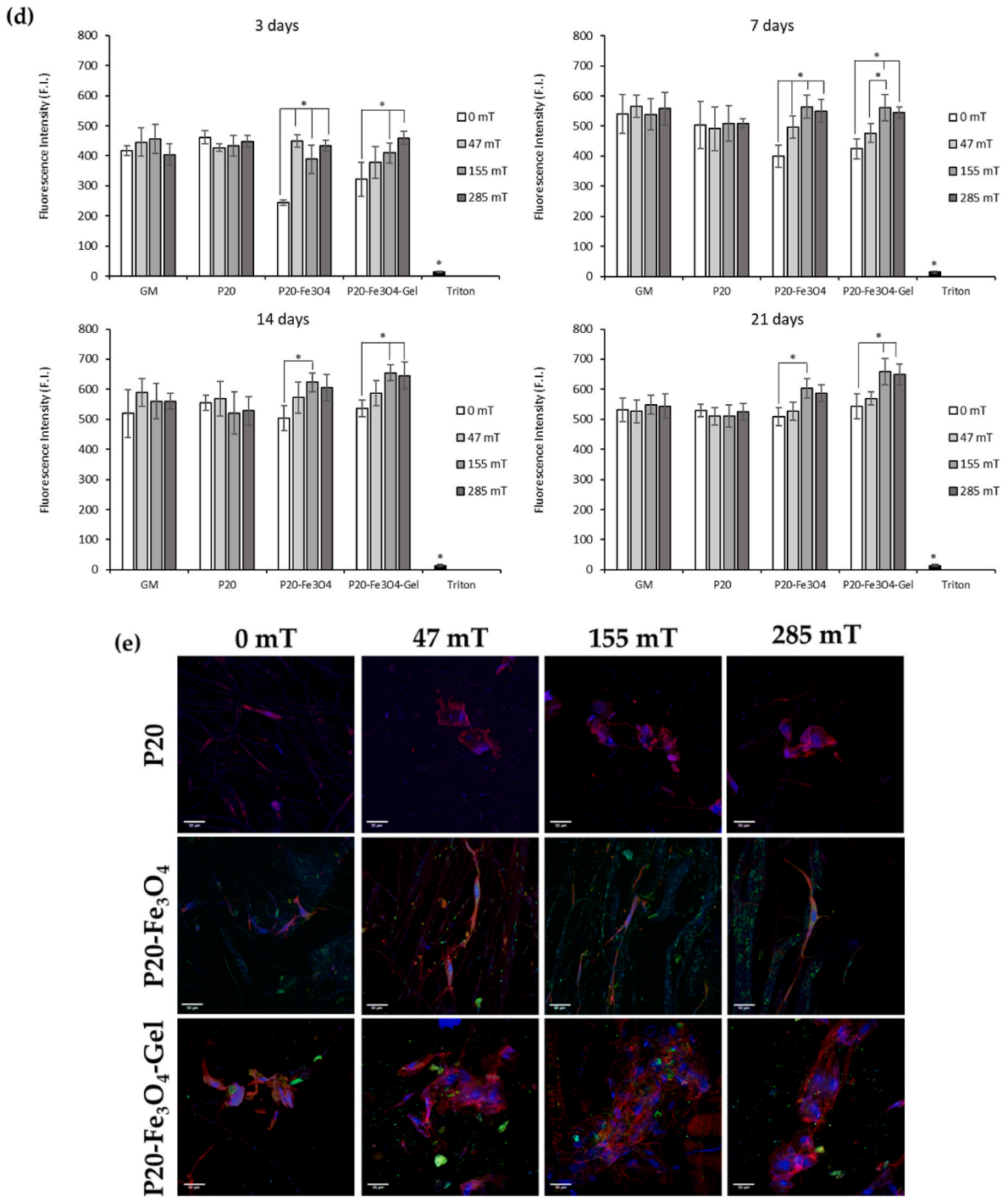

Fig. 8. (*continued*).

for tissue repair and regeneration, as stem cells respond to inflammatory cues by releasing pro-inflammatory mediators. In fact, stem cells can secrete cytokines, such as TNF-α and IL-1b, and chemokines that modulate immune response, influencing inflammation and tissue repair processes [59,60]. In particular, inflammation drives the mobilization of stem cells from their niches, enhancing their availability for tissue repair [59]. Conversely, while stem cells can produce inflammatory factors beneficial for tissue repair, excessive inflammation can lead to detrimental effects, such as chronic inflammation and tissue degeneration, highlighting the need for a balanced inflammatory response in stem cell therapy and regenerative medicine [61]. For these reasons, a preliminary evaluation *in vitro* on the proinflammatory immune response was performed on hASC cells after the contact with the scaffolds, in order to assure the avoidance of the risk of excessive inflammation and unbalanced tissue repair.

The pro-inflammatory immune response of the cells was evaluated by ELISA assay after 21 days of contact with the scaffolds with and without the application of the magnetic fields (Fig. 9). LPS was used as positive control, Triton as negative control. No significant secretion of TNF-α cytokine is visible after the contact with the scaffolds, meaning that the systems are safe, and they do not cause any excessive inflammatory reaction on stem cells.

Moreover, the hemocompatibility of P20-Fe_3O_4-Gel was evaluated by hemolysis test *in vitro,* by incubating the samples with fresh blood. As

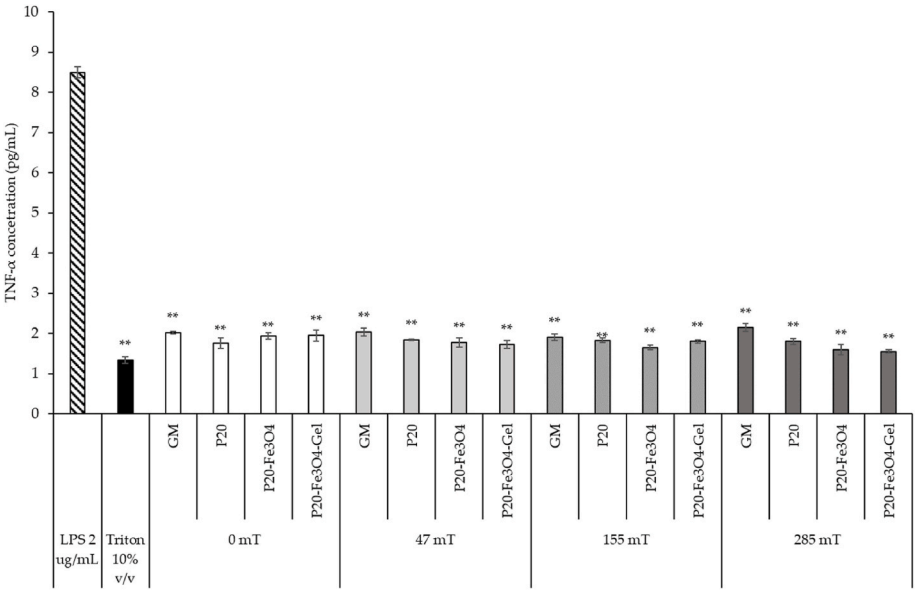

Fig. 9. TNF-α cytokine concentrations (pg/mL) secreted by the cells after 21 days of contact with the scaffolds, with and without external magnetic stimulatio (GM: growth medium; LPS: lipopolysaccharide) (mean values ± sd; n = 6). ANOVA one-way; Scheffé test ($p \leq 0.05$), ** indicates statistical differences with the cells treated with LPS 2 μg/mL ($p \leq 0.01$).

shown in Table 3, the scaffold is characterized by hemocompatibility properties. In fact, the hemolysis rate results lower than 5 %, suggesting that no hemolysis occurred [62,63].

3.8. *In vivo efficacy evaluation*

The *in vivo* efficacy of the scaffolds was investigated in a murine model; biopsies of intact tendon (Fig. 10a) and of the lesion treated with traditional suture alone (Fig. 10b–f,l) and combined with an external magnetic field of 155 mT ± 10 (Fig. 10c–g,m) were also taken as positive control.

In Fig. 10a, the healthy tendon shows fibrous connective tissue with parallel bundles. The fundamental substance is anistic and not very abundant, therefore not visible. The bundles of collagen fibers arranged in parallel are clearly visible, according to the lines of force to which the tendon is subjected. Rare cells, in particular tenocyte and tenoblasts, are arranged peripherally at the border with the surrounding connective tissue (endotenonium).

Fig. 10b–f,l show the tendon tissue treated with traditional suture alone after 1, 3, and 6 weeks respectively. After 1 week, an area affected by inflammatory cells is still evident in the central part of the tendon, mostly polymorphonuclear leukocytes and monocytes-macrophages which are completing the removal of necrotic tissues. This represents the end of the inflammatory phase, and the beginning pf proliferative phase. After 3 weeks, the inflammatory cells disappear and the structure of the tendon appears rebuilt, with the collagen fibers reorganizing themselves along the longitudinal axis. After 6 weeks, remodeling begins, leading to the consolidation of the structure and the restoration of the tensile strength of the tendon.

Fig. 10c–g,m show the tendon tissue treated with traditional suture combined with the external magnetic field after 1, 3, and 6 weeks respectively. After 1 week, an area affected by inflammatory cells (polymorphonuclear cells and monocytes-macrophages) and neoangiogenesis is evident, representing the inflammatory phase. After 3 weeks, proliferative phase begins. Both inflammatory cells and tenocytes/tenoblasts, which are rebuilding the matrix, are still abundant. The orientation of the newly formed collagen is not yet along the longitudinal axis. After 6 weeks, the cells disappear, and the collagen is orienting itself.

Fig. 10d–h,n show the tendon tissue treated with P20-Fe_3O_4-Gel scaffold alone after 1, 3, and 6 weeks respectively. After 1 week, the injured area is affected by inflammatory cells and tenoblasts/tenocytes that synthesize collagen and amorphous matrix, representing the end of the inflammatory phase, and the beginning of the proliferative phase. The proliferative phase continues after 3 weeks, since the inflammatory cells are no more visible, and the tendon structure appears rebuilt, with the collagen fibers reorganizing themselves along the longitudinal axis. After 6 weeks, remodeling phase begins, leading to the consolidation of the structure and the restoration of the tensile strength of the tendon.

Fig. 10e–i,o show the tendon tissue treated with P20-Fe_3O_4-Gel scaffold combined with the external magnetic field after 1, 3, and 6 weeks respectively. Interestingly, after 1 week of treatment the damaged area is already compacting, and, unlike the other samples, in this case the lesion is completely closed, and already in the proliferative phase. After 3 weeks newly formed collagen appears already oriented. After 6 weeks, the collagen is organizing itself along the longitudinal axis, leading to the consolidation of the structure and the restoration of the tensile strength of the tendon. All phases of treatment do not show degenerative events nor adipocyte infiltrations [64]. More importantly, no sign of inflammatory process was recognizable after 6 weeks of treatment, with no leukocyte recruitment or foreign body response.

An important issue is related to the implant's degradation, since it should degrade within the three months of treatment following the surgery in order to guarantee structural support, mimicking the native ECM, stimulating the cells homing and proliferation and potentially reducing medical complications. From the histology performed after 6 weeks, it is possible to observe that no scaffold residual is visible after the treatment, suggesting that *in vivo* scaffold's degradation is more rapid probably due to its replacement with native tissue.

These results highlight the potential of P20-Fe_3O_4-Gel scaffold in combination with an external magnetic field to speed up the tendon healing process.

Another important issue could involve the possible accumulation of Fe_3O_4 NPs in the body. It is already known that the MNPs primarily

Table 3
P20-Fe_3O_4-Gel HR%.

Scaffold	HR%
P20-Fe_3O_4-Ge	0.77 ± 0.50

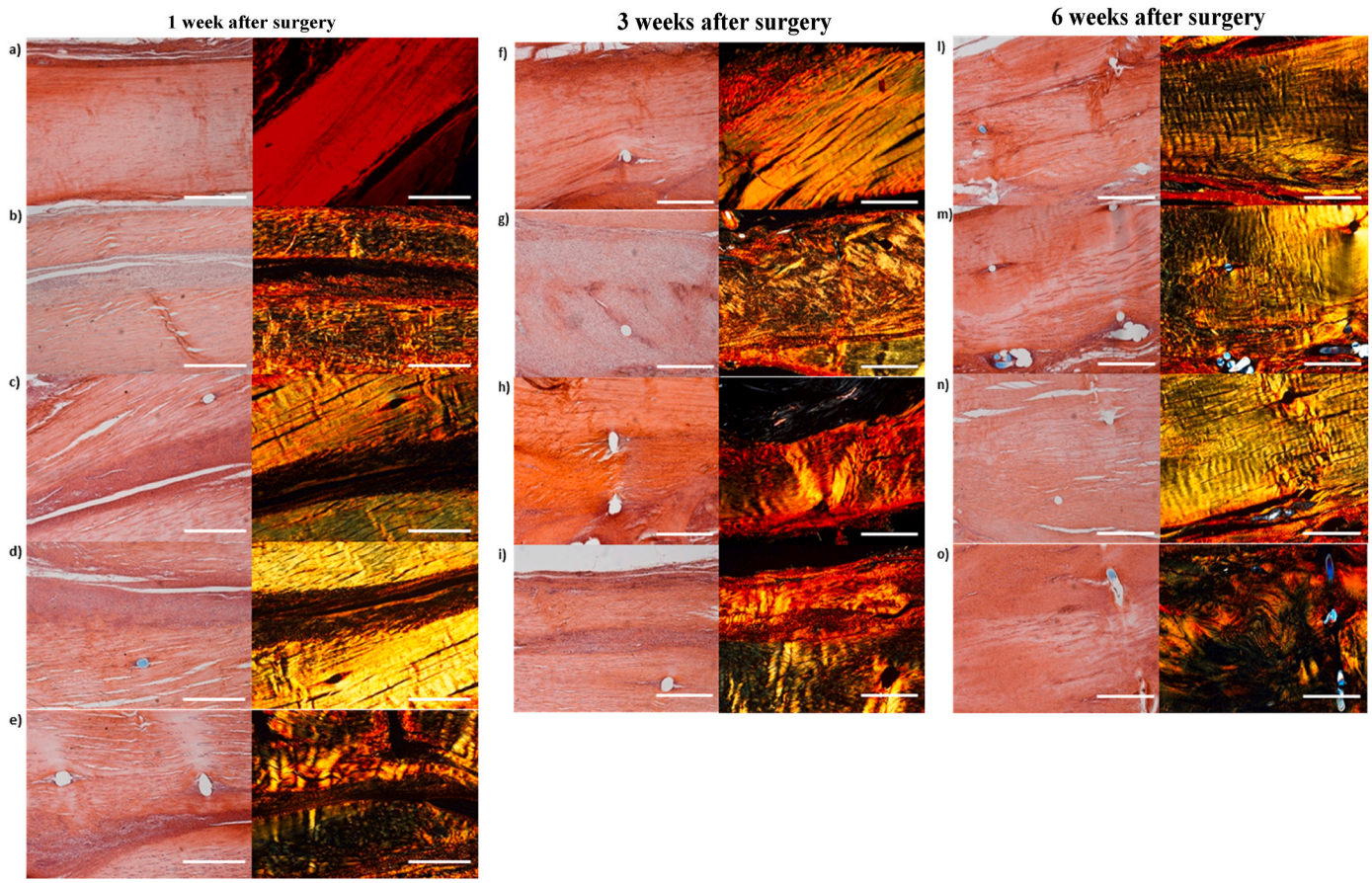

Fig. 10. H&E and PSR sections of the (a) intact tendon, (b) lesion treated with traditional suture after 1 week, (c) lesion treated with traditional suture combined with magnetic field after 1 week, (d) scaffold implant after 1 week, (e) scaffold implant combined with magnetic field after 1 week, (f) lesion treated with traditional suture after 3 weeks, (g) lesion treated with traditional suture combined with magnetic field after 3 weeks, (h) scaffold implant after 3 weeks, (i) scaffold implant combined with magnetic field after 3 weeks, (l) lesion treated with traditional suture after 6 weeks, (m) lesion treated with traditional suture combined with magnetic field after 6 weeks, (n) scaffold implant after 6 weeks, and (o) scaffold implant combined with magnetic field after 6 weeks. Original magnification: 5 × . Each micrograph frame has a width of 1780 μm (scale bar: 500 μm).

accumulate in the spleen (84.4 %) and liver (11.4 %), where they undergo metabolic processes [65]. In particular, their metabolism *in vivo* seems closely linked to the release of iron ions (Fe^{2+} and Fe^{3+}) as they undergo dissolution within cells. These released iron ions are processed through the body's natural iron metabolism pathways, involving binding to proteins like ferritin and transferrin, which facilitate their transport and storage in tissues, such as the liver and spleen [66]. Additionally, studies have shown that MNPs and their degraded components show low toxicity and do not cause permanent organs damage in low concentrations, being excreted from the body via both hepatobiliary and renal pathways, highlighting their safety profile [67,68]. In fact, concentrations in the range of 0.1–1 mg/kg body weight for intravenous administration and 1–10 mg/kg for oral administration are generally considered safe without significant toxic effects in many *in vivo* models, underlining the safety of the MNPs concentration loaded into P20-Fe_3O_4-Gel scaffold. Talesh et al. orally administered iron oxide NPs at doses of 50, 500, and 5000 mg/kg for five days in rats. The findings indicated that toxicity was dose-dependent, with higher doses leading to more pronounced adverse effects, such as lethargy, ataxia, anorexia, depression, and respiratory arrhythmia. However, the lower dose (50 mg/kg) administration had no consequent toxicity compared to the control group [69]. Similarly, Kumari et al. investigated repeated oral dosing of MNPs at 30, 300, and 1000 mg/kg in rats over 28 days, showing that the lower dose of 30 mg/kg did not cause toxicity [70].

4. Conclusion

Fibrous scaffolds based on PHB doped with magnetite and enriched with Gel were successfully manufactured with a centrifugal spinning. It was possible to develop fibers in aligned conformation able to mimic the tendon fascicles. The Fe_3O_4@OA NPs were successfully embedded into the fibrous matrix, leading to an increase of the scaffolds rigidity, while the Gel led to an increase in the surface wettability, which should result in a more favorable surface for the cells adhesion. The scaffolds were characterized by a superparamagnetic behavior that should guarantee a precise remote control over their functions. Moreover, the weight loss test performed for 12 weeks suggested a slow degradation rate that should guarantee a structural support during the entire tissue regeneration. Furthermore, the negligible iron release should decrease the risk of toxicity related to nanomaterials. It was possible to investigate the effect of static magnetic fields of different extent on the cells behavior when combined to the scaffolds. These findings should contribute to the understanding of the mechanisms of external magnetic mechanostimulation. The scaffolds enriched with Fe_3O_4@OA NPs promoted the cell proliferation, in particular when combined with the application of external magnetic fields of 155 and 285 mT. Moreover, the Gel also seemed effective since the cells were able to grow better in respect to the other scaffolds. The application of the magnetic field onto the scaffolds enriched with Fe_3O_4@OA NPs also led to a significant increase in the cell alignment onto the matrix. More importantly, hASCs cells were able to differentiate and produce collagen I matrix when the NPs-doped

scaffolds were combined with the external magnetic stimulation. Furthermore, the scaffolds did not cause any inflammatory reaction, and they resulted hemocompatible.

Finally, the *in vivo* efficacy evaluation demonstrated that P20-Fe_3O_4-Gel scaffold combined with the external magnetic stimulation led to the complete healing of the lesion after just 1 week of treatment. On the contrary, in the tendons treated with traditional suture and with the scaffold alone, the lesion was still visible after 1 week.

In conclusion, scaffolds based on PHB and doped with Gel and Fe_3O_4@OA NPs represent an interesting tool to enhance the tendon tissue regeneration and stimulate a deeper tissue regeneration, when combined with an external magnetic field, also deepening the actual knowledge on the use of static magnetic fields.

CRediT authorship contribution statement

Eleonora Bianchi: Writing – review & editing, Writing – original draft, Validation, Software, Methodology, Investigation, Formal analysis, Data curation, Conceptualization. **Manuel Bañobre-Lopez:** Validation, Resources, Methodology. **Marco Ruggeri:** Validation, Resources. **Elena Del Favero:** Writing – original draft, Investigation, Data curation. **Barbara Vigani:** Visualization, Resources. **Caterina Ricci:** Investigation. **Cinzia Boselli:** Investigation. **Antonia Icaro Cornaglia:** Investigation. **Martin Albino:** Writing – review & editing, Investigation. **Claudio Sangregorio:** Visualization, Resources. **Alessandro Lascialfari:** Writing – review & editing, Visualization. **Jessica Zanovello:** Investigation. **Eugenio Jannelli:** Investigation. **Francesco Claudio Pavesi:** Visualization. **Silvia Rossi:** Supervision, Resources, Funding acquisition. **Luca Casettari:** Visualization, Resources. **Giuseppina Sandri:** Writing – review & editing, Writing – original draft, Supervision, Resources, Methodology, Funding acquisition, Conceptualization.

Ethics approval statement

All animal experiments were carried out in full compliance with the standard international ethical guidelines (European Communities Council Directive 2010/63/EU). The study protocol was approved by the Local Institutional Ethics Committee of the University of Pavia for the use of animals and by ISS (Istituto Superiore di Sanità).

Funding

This research did not receive any specific grant from funding agencies in the public, commercial, or not-for-profit sectors.

Declaration of competing interest

The authors declare that they have no known competing financial interests or personal relationships that could have appeared to influence the work reported in this paper.

Acknowledgements

The authors wish to thank Dr. Bjorn Vergauwen and Dr. Jan De Merlier of Rousselot for providing the Gel. The authors also thank the project NODES (MUR – M4C2 1.5 of PNRR funded by the European Union - NextGenerationEU (Grant agreement no. ECS00000036) for funding EB grant and the INFN research project MATHER3D for funding A.L. and M.A. The authors acknowledge ESRF (Grenoble, Fr) for beamtime allocation and financial support for x-ray experiments (MD-1406 2023), and ID02 and PSCM staffs for precious technical assistance. The authors also acknowledge the animal facility “Centro di servizio per la gestione unificata delle attivit'a di stabulazione e di radiobiologia” of the University of Pavia (Italy) to host the animals and the OPBA of the University of Pavia for support in animal protocol drawing up.

Appendix A. Supplementary data

Supplementary data to this article can be found online at https://doi.org/10.1016/j.mtbio.2025.101699.

Data availability

Data will be made available on request.

References

[1] S. Steinmann, C.G. Pfeifer, C. Brochhausen, D. Docheva, Spectrum of tendon pathologies: triggers, trails and end-state, Int. J. Mol. Sci. 21 (2020) 844, https://doi.org/10.3390/ijms21030844.
[2] S. Ruiz-Alonso, M. Lafuente-Merchan, J. Ciriza, L. Saenz-del-Burgo, Tendon tissue engineering: cells, growth factors, scaffolds and production techniques, J. Contr. Release 10 (2021) 448–486, https://doi.org/10.1016/j.jconrel.2021.03.040.
[3] D.S. Morais, J. Torres, R.M. Guedes, M.A. Lopes, Current approaches and future trends to promote tendon repair, Ann. Biomed. Eng. 43 (2015) 2025–2035, https://doi.org/10.1007/s10439-015-1369-5.
[4] E. Bianchi, M. Ruggeri, S. Rossi, B. Vigani, D. Miele, M.C. Bonferoni, G. Sandri, F. Ferrari, Innovative strategies in tendon tissue engineering, Pharmaceutics 13 (2021) 89, https://doi.org/10.3390/pharmaceutics13010089.
[5] J.P.K. Armstrong, M.M. Stevens, Using remote fields for complex tissue engineering, Trends Biotechnol. 38 (2020) 254–263, https://doi.org/10.1016/j.tibtech.2019.07.005.
[6] E. Bianchi, A. Faccendini, E. Del Favero, C. Ricci, L. Caliogna, B. Vigani, F. C. Pavesi, C. Perotti, R.M.A. Domingues, M.E. Gomes, S. Rossi, G. Sandri, Topographical and compositional gradient tubular scaffold for bone to tendon interface regeneration, Pharmaceutics 14 (2022) 2153, https://doi.org/10.3390/pharmaceutics14102153.
[7] Y. Li, D. Ye, M. Li, M. Ma, N. Gu, Adaptive materials based on iron oxide nanoparticles for bone regeneration, ChemPhysChem 17 (2018) 1965–1979, https://doi.org/10.1002/cphc.201701294.
[8] Z. Huang, Y. He, X. Chang, J. Liu, L. Yu, Y. Wu, Y. Li, J. Tian, L. Kang, D. Wu, H. Wang, Z. Wu, G. Qiu, A magnetic iron oxide/polydopamine coating can improve osteogenesis of 3D-printed porous titanium scaffolds with a static magnetic field by upregulating the TGFβ-smads pathway, Adv Healthc Mater 9 (2020) 2000318, https://doi.org/10.1002/adhm.202000318.
[9] M.R. Bashir, L. Bhatti, D. Marin, R.C. Nelson, Emerging applications for ferumoxytol as a contrast agent in MRI, J. Magn. Reson. Imag. 41 (2015) 884–898, https://doi.org/10.1002/jmri.24691.
[10] R. Sheng, Y. Jiang, L.J. Backman, W. Zhang, J. Chen, The application of mechanical stimulations in tendon tissue engineering, Stem Cell. Int. (2020) 8824783, https://doi.org/10.1155/2020/8824783.
[11] T. Kito, R. Shibata, M. Ishii, H. Suzuki, T. Himeno, Y. Kataoka, Y. Yamamura, T. Yamamoto, N. Nishio, S. Ito, Y. Numaguchi, T. Tanigawa, J.K. Yamashita, N. Ouchi, H. Honda, K. Isobe, T. Murohara, iPS cell sheets created by a novel magnetite tissue engineering method for reparative angiogenesis, Sci. Rep. 3 (2013) 14188, https://doi.org/10.1038/srep01418.
[12] H. Akiyama, A. Ito, M. Sato, Y. Kawabe, M. Kamihira, Construction of cardiac tissue rings using a magnetic tissue fabrication technique, Int. J. Mol. Sci. 11 (2010) 2910–2920, https://doi.org/10.3390/ijms11082910.
[13] K. Shimizu, A. Ito, T. Yoshida, Y. Yamada, M. Ueda, H. Honda, Bone tissue engineering with human mesenchymal stem cell sheets constructed using magnetite nanoparticles and magnetic force, J. Biomed. Mater. Res. Part B Appl. Biomater. 82B (2007) 471–480, https://doi.org/10.1002/jbm.b.30752.
[14] Y. Yamamoto, A. Ito, H. Fujita, E. Nagamori, Y. Kawabe, M. Kamihira, Functional evaluation of artificial skeletal muscle tissue constructs fabricated by a magnetic force-based tissue engineering technique, Tissue Eng Pt A 17 (2011) 107–114, https://doi.org/10.1089/ten.tea.2010.0312.
[15] A.I. Gonçalves, M.T. Rodrigues, M.E. Gomes, Tissue-engineered magnetic cell sheet patches for advanced strategies in tendon regeneration, Acta Biomater. 63 (2017) 110–122, https://doi.org/10.1016/j.actbio.2017.09.014.
[16] A.R. Tomás, A.I. Gonçalves, E. Paz, P. Freitas, R.M.A. Domingues, M.E. Gomes, Magneto-mechanical actuation of magnetic responsive fibrous scaffolds boosts tenogenesis of human adipose stem cells, Nanoscale 11 (2019) 18255–18271, https://doi.org/10.1039/c9nr04355a.
[17] J. Yang, J. Wu, Z. Guo, G. Zhang, H. Zhang, Iron oxide nanoparticles combined with static magnetic fields in bone remodeling, Cells 11 (2022) 3298, https://doi.org/10.3390/cells11203298.
[18] T. Freier, Biopolyesters in tissue engineering applications, in: C. Werner (Ed.), Polymers for Regenerative Medicine, vol. 203, Springer, Berlin, Heidelberg, 2006, pp. 1–61.
[19] Z.A. Raza, S. Abid, I.M. Banat Polyhydroxyalkanoates, Characteristics, production, recent developments and applications, Int. Biodeterior. Biodegrad. 126 (2018) 45–56, https://doi.org/10.1016/j.ibiod.2017.10.001.
[20] S.F. Williams, D.P. Martin, D.M. Horowitz, O.P. Peoples, PHA applications: addressing the price performance issue I. Tissue engineering, Int. J. Biol. Macromol. 25 (1999) 111–121, https://doi.org/10.1016/s0141-8130(99)00022-7.
[21] E. Bugnicourt, P. Cinelli, A. Lazzeri, V. Alvarez, Polyhydroxyalkanoate (PHA): review of synthesis, characteristics, processing and potential applications in

packaging, Express Plym Lett 8 (2014) 791–808, https://doi.org/10.3144/expresspolymlett.2014.82.
[22] V.I. Sevastianov, N.V. Perova, E.I. Shishatskaya, G.S. Kalacheva, T.G. Volova, Production of purified polyhydroxyalkanoates (PHAs) for applications in contact with blood, J. Biomater. Sci. Polym. Ed. 14 (2003) 1029–1042, https://doi.org/10.1163/156856203769231547.
[23] E.E. Kaufman, N. Relkin, T. Nelson, Regulation and properties of an NADP+ oxidoreductase which functions as a gammahydroxybutyrate dehydrogenase, J. Neurochem. 40 (1983) 1639–1646, https://doi.org/10.1111/j.1471-4159.1983.tb08137.x.
[24] J. Hahn, A. Breier, H. Brünig, G. Heinrich, Long-term hydrolytic degradation study on polymer-based embroidered scaffolds for ligament tissue engineering, JIT (2018), https://doi.org/10.1177/1528083716686940.
[25] N. Jain, G.K. Jain, S. Javed, Z. Iqbal, S. Talegaonkar, F.J. Ahmad, R.K. Khar, Recent approaches for the treatment of periodontitis, Drug Discov. Today 13 (2008) 932–943, https://doi.org/10.1016/j.drudis.2008.07.010.
[26] M. Budai-Szucs, M. Ruggeri, A. Faccendini, A. Léber, S. Rossi, G. Varga, M. C. Bonferoni, P. Vályi, K. Burián, E. Csányi, G. Sandri, F. Ferrari, Electrospun scaffolds in periodontal wound healing, Polymers 13 (2021) 307, https://doi.org/10.3390/polym13020307.
[27] E. Bianchi, E. Del Favero, C. Ricci, Biomechano-responsive polymeric scaffolds for tendon regeneration, European Synchrotron Radiation Facility (2023), https://doi.org/10.15151/ESRF-ES-1351189712.
[28] E. Bianchi, M. Ruggeri M, B. Vigani, E. Del Favero, C. Ricci, C. Boselli, A. Icaro Cronaglia, C. Viseras, S. Rossi, G. Sandri, Cerium oxide and chondroitin sulfate doped polyurethane scaffold to bridge tendons, ACS Appl. Mater. Interfaces 15 (22) (2023) 26510–26524, https://doi.org/10.1021/acsami.3c06144.
[29] M. Hordé, J. Fouchard, X. Laffray, C. Blavet, V. Béréziat, C. Lagathu, L. Gaut, D. Duprez, E. Havis, Human adipose stromal cells differentiate towards a tendon phenotype with adapted visco-elastic properties in a 3D-culture system, bioRxiv 25 (2024) 591060, https://doi.org/10.1101/2024.04.25.591060.
[30] Q. Long, W. Zhang, C. Liu, H. Zheng, M. Wang, Z. Cao, Y. Sun, Q. Mo, L. J. Backman, J. Huang, J. Chen, Enhancing tendon regeneration: investigating the impact of topography on the secretome of adipose-derived stem cells, Res Sq (2023), https://doi.org/10.21203/rs.3.rs-2732911/v1.
[31] C. Yuan, W. Song, X. Jiang, Y. Wang, C. Li, W. Yu, Y. He, Adipose-derived stem cell-based optimization strategies for musculoskeletal regeneration: recent advances and perspectives, Stem Cell Res. Ther. 15 (2024) 91, https://doi.org/10.1186/s13287-024-03703-6.
[32] A. Montes, A. Mauro, A. Cerveró-Varona, G. Prencipe, M. El Khatib, U. Tosi, G. Wouters, J. Stöckl, V. Russo, B. Barboni, Novel stem cell strategies for tendon regenerative medicine, Orthop Procs 106-B (SUPP_2) (2024) 12, https://doi.org/10.1302/1358-992X.2024.2.012.
[33] J. Meng, Y. Zhang, X. Qi, H. Kong, C. Wang, C. Xu, S. Xie, N. Gu, H. Xu, Paramagnetic nanofibrous composite films enhance the osteogenic responses of pre-osteoblastcells, Nanoscale 12 (2010), https://doi.org/10.1039/C0NR00178C.
[34] E. Bianchi, M. Ruggeri, B. Vigani, C. Totaro Fila, A. Icaro Cornaglia, C. Boselli, C. Viseras, S. Rossi, G. Sandri, Gas foamed scaffolds as smart 3D structures in skin tissue engineering, J. Drug Deliv. Sci. Technol. 95 (2024) 105541, https://doi.org/10.1016/j.jddst.2024.105541.
[35] Y. Duan, K. Li, H. Wang, T. Wu, Y. Zhao, H. Li, H. Tang, W. Yang, Preparation and evaluation of curcumin grafted hyaluronic acid modified pullulan polymers as a functional wound dressing material, Carohydr Polym 238 (2020) 116195, https://doi.org/10.1016/j.carbpol.2020.116195.
[36] M.H. Amini, J. Martin, H. Kisana, M. McKee, Early improvement in outcomes after rotator cuff repair is predictive of greater final improvement, Arthroscopy 36 (2023), https://doi.org/10.1016/j.arthro.2023.01.030.
[37] H. Kabir, N. Garg, Machine learning enabled orthogonal camera goniometry for accurate and robust contact angle measurements, Sci. Rep. 13 (2023) 1497, https://doi.org/10.1038/s41598-023-28763-1.
[38] T. Pesqueira, R. Costa-Almeida, M.E. Gomes, Uncovering the effect of low-frequency static magnetic field on tendon-derived cells: from mechanosensing to tenogenesis, Sci. Rep. 7 (2017) 10948, https://doi.org/10.1038/s41598-017-11253-6.
[39] A.I. Goncalves, M.T. Rodrigues, M.E. Gomes, Tissue-engineered magnetic cell sheet patches for advanced strategies in tendon regeneration, Acta Biomater. 63 (2017) 110–122, https://doi.org/10.1016/j.actbio.2017.09.014.
[40] J. Dulińska-Litewka, A. Łazarczyk, P. Hałubiec, O. Szafrański, K. Karnas, A. Karewicz, Superparamagnetic iron oxide nanoparticles—current and prospective medical applications, Materials 12 (2019) 617, https://doi.org/10.3390/ma12040617.
[41] S. Paliwal, S. Sharma. Functionalized Magnetic Nanoparticles for Tissue Engineering. *Functionalized Magnetic Nanoparticles For Theranostic Applications* **2024**, Eds M. Pandey, K. Deshmukh, C.M. Hussain. Doi: 10.1002/9781394172917.ch9.
[42] J.V. Cardoza, Z. Ali, S. Simon, D. Thakkar, S.S. George, S.P. Isaac, The role of nanoparticles in accelerating tissue recovery and inflammation control in physiotherapy practices, Cureus 16 (2024) e73540, https://doi.org/10.7759/cureus.73540.
[43] M. Smiri, F. Guey, H. Chemingui, A.B. Dekhil, S. Elarbaoui, A. Hafiane, Remove of humic acid from water using magnetite nanoparticles, Eur. J. Chem. 1 (2020) 1–6, https://doi.org/10.24018/ejchem.2020.1.4.9.
[44] X.N. Pham, T.P. Nguyen, T.N. Pham, T.T.N. Tran, T.V.T. Tran, Synthesis and characterization of chitosan-coated magnetite nanoparticles and their application in curcumin drug delivery, Adv. Nat. Sci. Nanosci. Nanotechnol. 7 (2016) 045010, https://doi.org/10.1088/2043-6262/7/4/045010.
[45] R. Qadir, J. Hossan, A. Gafur, M.M. Karim, Preparation and characterization of gelatin-hydroxyapatite composite for bone tissue engineering, Int. J. Eng. Sci. 14 (2014) 24.
[46] S. Shankar, X. Teng, J.W. Rhim, Properties and characterization of agar/CuNP bionanocomposite films prepared with different copper salts and reducing agents, Carbohydr. Polym. 114 (2014) 484–492, https://doi.org/10.1016/j.carbpol.2014.08.036.
[47] W.L. Lim, L.L. Liau, M.H. Ng, S.R. Chowdhury, J.X. Law, Current progress in tendon and ligament tissue engineering, Tissue Eng. Regen. Med. 16 (2019) 549–571, https://doi.org/10.1007/s13770-019-00196-w.
[48] Y. Meng, C. Shi, B. Hu, J. Gong, X. Zhong, X. Lin, X. Zhang, J. Liu, C. Liu, H. Xu, External magnetic field promotes homing of magnetized stem cells following subcutaneous injection, BMC Cell Biol. 18 (2017) 24, https://doi.org/10.1186/s12860-017-0140-1.
[49] B.A. Saletnik, A. Puchalska-Sarna, A. Saletnik, T. Lipa, B. Dobrzański, C. Puchalski, Static magnetic fields as a factor in modification of tissue and cell structure: a review, Int. Agrophys. 38 (2024), https://doi.org/10.31545/intagr/176998.
[50] R. Mousavizadeh, V.C. West, K.L. Inguito, D.M. Elliott, J. Parreno, The application of mechanical load onto mouse tendons by magnetic restraining represses Mmp-3 expression, BMC Res. Notes 16 (2024) 127, https://doi.org/10.1186/s13104-023-06413-z.
[51] A. Vinhas, M.T. Rodrigues, A.I. Gonçalves, M.E. Gomes, Immunomodulatory behavior of tendon magnetic cell sheets can be modulated in hypoxic environments under magnetic stimulus, ACS Appl. Mater. Interfaces 16 (2024) 34. https://pubs.acs.org/doi/10.1021/acsami.4c08154.
[52] K. Harasimov, M. Schuh, Actin disassembly: how to contract without motors? Curr. Biol. 28 (2018) R275 https://doi.org/10.1016/j.cub.2018.02.019.
[53] Y. Shou, X.Y. Teo, K.Z. Wu, B. Bai, A.R.K. Kumar, J. Low, Z. Le, A. Tay, Dynamic stimulations with bioengineered extracellular matrix-mimicking hydrogels for mechano cell reprogramming and therapy, Adv. Sci. 10 (2023) e2300670, https://doi.org/10.1002/advs.202300670.
[54] M. Ahearne, Introduction to cell-hydrogel mechanosensing. Interface, Focus 4 (2014) 20130038, https://doi.org/10.1098/rsfs.2013.003.
[55] P. Delmas, B. Coste, Mechano-gated ion channels in sensory systems, Cell 155 (2013) 278, https://doi.org/10.1016/j.cell.2013.09.026.
[56] F. Martino, A.R. Perestrelo, V. Vinarský, S. Pagliari, Cellular mechanotransduction: from tension to function, Front. Physiol. 9 (2018) 824, https://doi.org/10.3389/fphys.2018.00824.
[57] Y.-C. Chang, J.-W. Wu, C.-W. Wang, A.C.-C. Jang, Hippo signaling-mediated mechanotransduction in cell movement and cancer metastasis front, Mol. Biosci. 6 (2019) 157, https://doi.org/10.3389/fmolb.2019.00157.
[58] E. Bianchi, M. Ruggeri, B. Vigani, C. Aguzzi, S. Rossi, G. Sandri, Synthesis and use of thermoplastic polymers for tissue engineering purposes, Int J Pharm X 9 (2025) 100313, https://doi.org/10.1016/j.ijpx.2024.100313.
[59] H.-H. Chang, Y.-S. Liou, D.-S. Sun, Unraveling the interplay between inflammation and stem cell mobilization or homing: implications for tissue repair and therapeutics, TCMJ 36 (2024) 349–359, https://doi.org/10.4103/tcmj.tcmj_100_24.
[60] L. Wang, Y. Li, M. Xu, Z. Deng, Y. Zhao, M. Yang, Y. Liu, R. Yuan, Y. Sun, H. Zhang, H. Wang, Z. Qian, H. Kang, Regulation of inflammatory cytokine storms by mesenchymal stem cells, Front. Immunol. 12 (2021), https://doi.org/10.3389/fimmu.2021.726909.
[61] M. Tatullo, S. Rengo, G. Sammartino, M. Simeone, A. Valletta, R. Gasparro Inflammaging, Epigenetic damage, mitochondrial dysfunctions, and macrophage alterations are the main missing pieces in the complex mosaic of stem cell physiology, Discov. Med. 36 (2024) 1772–1779, https://doi.org/10.24976/Discov.Med.202436188.163.
[62] D.C. Manatunga, R.M.D. Silva, K.M.N.D. Silva, G.N. Malavige, D.T. Wijeratne, G. R. Williams, C.D. Jayasinghe, P.V. Udagama, Effective delivery of hydrophobic drugs to breast (MCF-7) and Liver (HepG2) cancer cells: a detailed investigation using cytotoxicity assays, fluorescence imaging and flow cytometry, Eur. J. Pharm. Biopharm. 128 (2018) 18–26, https://doi.org/10.1016/j.ejpb.2018.04.001.
[63] F. Wu, T. Xu, G. Zhao, S. Meng, M. Wan, B. Chi, C. Mao, J. Shen, Mesoporous silica nanoparticles-encapsulated agarose and heparin as anticoagulant and resisting bacterial adhesion coating for biomedical silicone. J, Langmuir 33 (2017) 5245–5252, https://doi.org/10.1021/acs.langmuir.7b00567.
[64] C. Lee, Orthopaedics and Trauma, vol. 35, 2021, pp. 274–281, https://doi.org/10.1016/j.mporth.2021.07.003.
[65] W. Zhang, S. huo, S. Deng, K. Min, C. Huang, H. Yang, L. Liu, L. Zhang, P. Zuo, L. Liu, G. Jiang, In vivo exposure pathways of ambient magnetite nanoparticles revealed by machine learning-aided single-particle mass spectrometry, Nano Lett. 24 (2024), https://doi.org/10.1021/acs.nanolett.4c01937.
[66] J. Nowak-Jary, B. Machnicka, In vivo biodistribution and clearance of magnetic iron oxide nanoparticles for medical applications, Int. J. Nanomed. 18 (2023) 4067–4100, https://doi.org/10.2147/IJN.S415063.
[67] S. Aboushoushah, W. Alshammari, R. Darwesh, N. Elbaily, Toxicity and biodistribution assessment of curcumin-coated iron oxide nanoparticles: multidose administration, Life Sci. 277 (2021) 119625, https://doi.org/10.1016/j.lfs.2021.119625.
[68] R. Enteshari Najafabadi, N. Kazemipour, A. Esmaeili, S. Beheshti, S. Nazifi, Using superparamagnetic iron oxide nanoparticles to enhance bioavailability of quercetin

in the intact rat brain, BMC Pharmacol Toxicol 19 (2018) 59, https://doi.org/10.1186/s40360-018-0249-7.

[69] S. Talesh, M.K. Koohi, E. Zayerzadeh, J. Hasan, M. Shabanian, Acute toxicity investigation regarding clinical and pathological aspects following repeated oral administration of iron oxide nanoparticles in rats, Nanomed Res J 4 (2019) 228–233, https://doi.org/10.22034/nmrj.2019.04.004.

[70] M. Kumari, S. Rajak, S.P. Singh, S.I. Kumari, P.U. Kumar, U.S.N. Murty, M. Mahboob, P. Grover, M.F. Rahman, Repeated oral dose toxicity of iron oxide nanoparticles: biochemical and histopathological alterations in different tissues of rats, J. Nanosci. Nanotechnol. 12 (2012) 2149–2159, https://doi.org/10.1166/jnn.2012.5796.